UNIVERSITÉ LIBRE DE BRUXELLES

BRUFACE BRUSSELS FACULTY OF ENGINEERING

VRIJE UNIVERSITEIT BRUSSEL

# Enabling fast-charging capabilities

## A perspective from battery-making processes

Alex Roig I Fornés

Master thesis submitted under the supervision of
Prof. Dr. Maitane Berecibar

Under the co-supervision of
Dr. Kamil Burak Dermenci and Emre Guney

Academic year
2024/2025

Master's thesis submitted in order to be awarded the Master's Degree in
Chemical and Materials Engineering

ECOLE
POLYTECHNIQUE
DE BRUXELLES

***DOCUMENT TO BE INCLUDED IN THE MASTER THESIS***

## CONSULTATION OF THE MASTER THESIS

I, the undersigned

NAME Roig I Fornés

FIRST NAME Alex

MASTER PROGRAM Master of Science in Chemical and Materials Engineering

MASTER THESIS TITLE Enabling fast-charging capabilities. A perspective from battery making processes

**AUTHORIZE*** X

**REFUSE***

(IN CASE OF REFUSAL, THIS DOCUMENT MUST BE COUNTERSIGNED BY THE MASTER THESIS SUPERVISOR)

*(* Delete as appropriate)*

Consultation of this master thesis by users of the libraries of the Université libre de Bruxelles.

If consultation is authorised, the undersigned hereby grants the Université libre de Bruxelles a free and non-exclusive licence, for the duration of the legal term of protection of the work, to reproduce and communicate to the public the above-mentioned work, on graphic or electronic media, in order to enable users of the libraries of the ULB and other institutions to consult it within the framework of inter-library loan.

Brussels, 27/05/2025

Signature of the student

Alex Roig Fornés

Signature of the supervisor
(only if consultation is refused)

# Abstract

The rapid growth of electric mobility has increased the demand for batteries capable of withstanding fast charging without compromising their performance or lifetime. The objective of this Master's Thesis is the optimization of cathode composition, loading, and mechanical pressure in lithium-ion batteries (LiBs) using NMC811-based cathodes, to enable fast charging.

A series of coin half-cell experiments were performed to analyze the effects of varying cathode composition, cathode loading, and cell mechanical pressure on specific capacity, charge transfer resistance, and capacity loss under fast-charging conditions. A systematic experimental design was employed to ensure consistent and comparable results. The experimental procedure involved the fabrication of coin and pouch cells, followed by electrochemical cycling tests and electrochemical impedance spectroscopy (EIS). Structural characterization of the cathode materials was performed using X-ray diffraction (XRD), which provided insights into their structural integrity and degradation mechanisms.

The findings reveal that a balanced cathode composition with at least 5 wt% polymer binder and an active material-to-conductive agent ratio of 17 is critical for maintaining fast charging (2C rate) and minimizing degradation. Additionally, cells with lower cathode loading outperformed those with higher loading, and applying mechanical pressure during assembly significantly enhanced electrochemical performance.

Furthermore, the effect of fast charging on the electrochemical performance of pouch full-cells with a graphite anode was studied. In this case, the pouch full-cells exhibited significantly higher charge transfer resistance and Warburg impedance compared to coin half-cells, which limited their ability to support fast-charging rates. These resistive and diffusional limitations hinder the efficient movement of lithium ions during high-rate charging. In contrast, the coin half-cells showed lower electrochemical resistance and better ion transport characteristics, enabling them to tolerate 2C charging conditions more effectively. The double-layer capacitance values were similar in both configurations, indicating comparable interfacial capacitance.

This work contributes to the development of faster-charging batteries and offers guidance for future studies aimed at improving electrode design for electric vehicle applications.

**Alex Roig I Fornés**

*Master of Science in Chemical and Materials Engineering*

**Academic Year:** 2024-2025

**Thesis title:** Enabling fast-charging capabilities. A perspective from battery-making processes

**Keywords:** Lithium-ion batteries, Fast charging, NMC811 cathode, Cathode properties, Electrochemical performance

# Contents

# List of Figures

**Chapter 1**



**Chapter 2**



**Chapter 3**



**Chapter 4**

**Appendices**

# List of Tables

# Chapter 1

# Introduction

## 1.1 Context

### 1.1.1 Worldwide Energy Problem

For decades, fossil fuels have been the dominant energy source, supporting industrial growth, transportation, and modern infrastructure. However, this reliance comes at a high cost. Fossil fuel consumption releases large amounts of greenhouse gases, contributing to climate change, air pollution, and environmental degradation. The urgent need to reduce these impacts has underscored the importance of transitioning to cleaner and more sustainable energy sources. Achieving this shift is essential not only for environmental preservation but also for fostering energy resilience and supporting a sustainable future [1].

In response to these challenges, renewable energy sources (RES), such as photovoltaics and wind turbines, have gained widespread adoption as alternatives to fossil fuels. These technologies offer clean and abundant energy, making them essential to global decarbonization strategies. However, the intermittent nature of RES introduces reliability and stability issues in the electric grid. Variations in sunlight and wind availability can cause fluctuations in power generation, complicating the continuous balance between electricity supply and demand.

To overcome these limitations and fully harness the potential of renewable energy, battery energy storage systems have emerged as a key enabling solution. By storing excess energy generated during peak production periods and delivering it when demand is high or generation is low, batteries enhance the operational flexibility and stability of modern power systems [2]. In this way, batteries not only support the large-scale integration of RES but also play a critical role in the broader transition toward a sustainable energy future.

Beyond grid applications, batteries are indispensable in today's world for powering a wide range of technologies. As global energy demand continues to grow, batteries have become critical enablers of technological advancement and sustainability. From smartphones and electric vehicles to renewable energy storage systems, they serve as the backbone of countless devices and applications that shape our daily lives. Their ability to store and deliver energy on demand facilitates convenience while also supporting the reduction of fossil fuel dependence and helping mitigate climate change.

The global trends in greenhouse gas (GHG) emissions serve as a stark reminder of the urgent need to transition toward sustainable energy practices. These trends, as illustrated in Figure 1.1, highlight the contributions of various sectors to total emissions over key years, underscoring the importance of decarbonizing energy-intensive activities. In this context, batteries emerge as a crucial solution not only for enabling the integration of renewable energy into the grid but also for supporting cleaner technologies in transportation, industry, and consumer electronics. Their development is therefore central to addressing the environmental challenges posed by fossil fuels and accelerating the shift toward a more sustainable energy future.

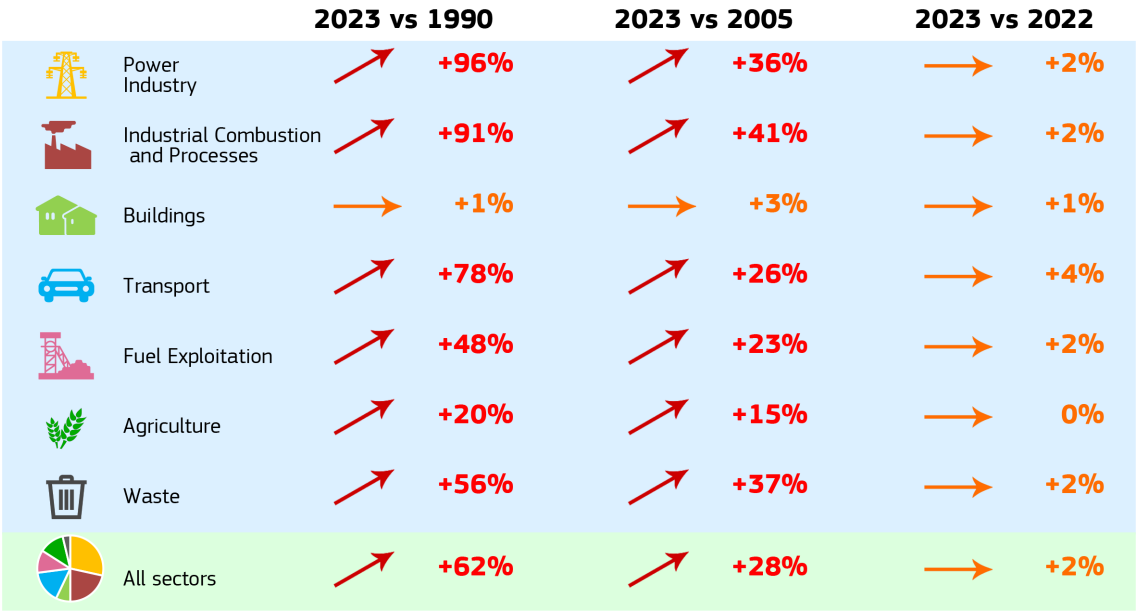


Figure 1.1: Global GHG emission trends by sector and key years [3].

### 1.1.2 E-Mobility: Transforming Transportation

As the world moves toward a more sustainable future, the demand for energy-efficient and environmentally friendly mobility solutions has surged, with batteries playing a pivotal role in this transition. By powering the rise of electric vehicles (EVs), batteries are transforming the future of transportation. EVs represent a significant shift away from conventional gasoline-powered cars, offering a cleaner alternative that reduces greenhouse gas emissions and the dependence on fossil fuels. LiB technologies are central to this revolution, which provide the energy storage capacity needed for efficient and long-range electric vehicle performance. This transition addresses the urgent need to combat climate change and reduce air pollution in urban areas, positioning batteries as the cornerstone of sustainable mobility.

Thus, great effort is being made to make this change possible, which can be seen in Figure 1.2, where the data published by the International Energy Agency (IEA) is shown on the global supply of electric cars. Electric cars accounted for around 18% of all cars sold in 2023, up from 14% in 2022 and only 2% 5 years earlier, in 2018. These trends indicate that growth remains robust as electric car markets mature [4].

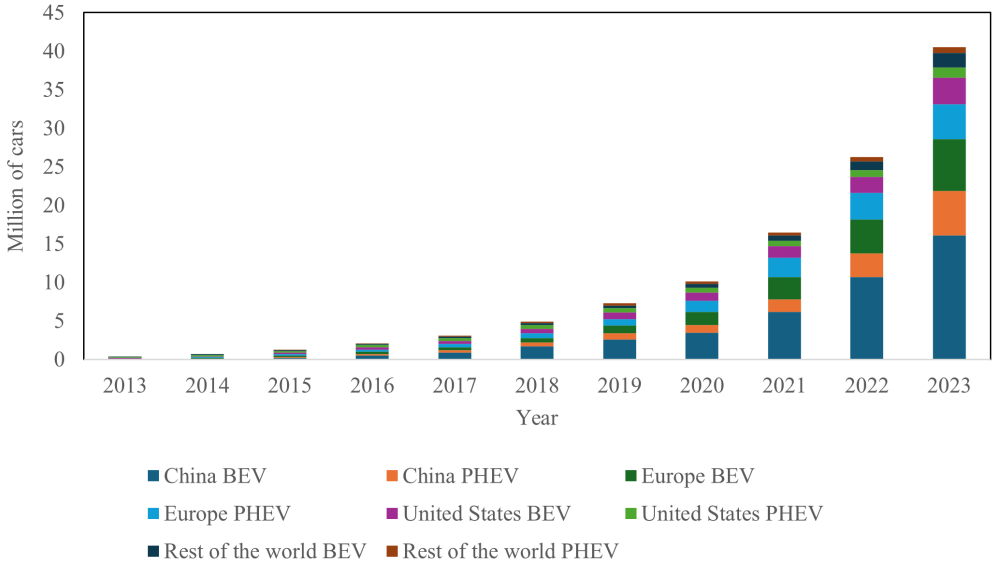


Figure 1.2: Global electric car stock (2013-2023) [4].

Both, battery electric vehicles (BEVs) and plug-in hybrid electrical vehicles (PHEVs), have experienced exponential growth, driven by advancements in battery technology, increasing environmental awareness, and supportive government policies. As adoption continues to rise, so too does the demand for faster, more efficient charging solutions, making the development of fast-charging batteries a critical focus for enabling the future of electric mobility.

## 1.2 Thesis Structure

This thesis is structured into five chapters:

Chapter 1 provides the background and motivation of the study. The importance of LiBs in fast-charging applications, particularly for electric vehicles, is introduced.

Following this, Chapter 2 presents a comprehensive review of the state-of-the-art in LiB technology, with a focus on fast charging and the associated degradation mechanisms. It explores the operating principles of LiBs, reviews common cathode and anode materials, and discusses how electrode architecture, such as loading, influences fast-charging performance. This chapter establishes the theoretical background necessary for understanding the challenges addressed in this study.

Next, Chapter 3 describes the experimental methodology used in this research. The electrode manufacturing process, the characterization techniques, and the testing protocols applied to assess battery performance under fast-charging conditions are detailed. The selection of materials, electrode preparation procedures, and electrochemical measurement techniques are discussed as well.

The results and their discussion are presented in Chapter 4, where the impact of cathode composition and loading, and other manufacturing parameters, on electrochemical performance and degradation are analyzed. Special attention is given to capacity fading, charge transfer resistance, and cycle life under fast-charging conditions.

Finally, Chapter 5 summarizes the key findings and contributions of this work. The main research questions are addressed, and the implications of the results are discussed. Additionally, recommendations for improving electrode design and manufacturing strategies to enhance fast-charging capabilities while mitigating degradation are provided. The thesis concludes with a discussion of potential future research directions in the field of LiB optimization.

# Chapter 2

# State of the art

## 2.1 Battery Types and Operation

Batteries convert chemical energy into electrical energy through redox (oxidation–reduction) reactions, known as electrochemical reactions. In the case of rechargeable batteries, this process is reversible: during charging, electrical energy is converted back into chemical energy and stored for later use. In addition to economic factors, certain requirements are necessary for a battery to be useful: its voltage should remain constant during discharge; it should have sufficient, typically high, capacity to supply current; and it must retain charge effectively, with a low self-discharge rate.

In practice, commercial or "real-world" batteries do not always perfectly meet the ideal criteria described above. Instead, they are designed to satisfy these requirements to the extent necessary for their specific application. For example, while some energy storage systems prioritize high energy density, others may focus on long cycle life or safety, depending on the intended use. Batteries are classified into two types: primary and secondary batteries [5].

### 2.1.1 Primary Batteries

Primary batteries, also known as non-rechargeable batteries, play a vital role in everyday's life due to their ability to provide a reliable and immediate energy source without the need for maintenance or recharging. Their applications span from consumer electronics to critical systems in healthcare and defence. Despite the growing interest in rechargeable technologies, primary batteries remain indispensable in many fields like medical implantation, aerospace, or military, thanks to their long shelf life and high energy density [6].

The most common types of primary batteries available today vary in their chemistry and performance characteristics, each suited to specific applications based on energy density, shelf life, and cost. The main types include:

- **Alkaline batteries**. The $Zn-MnO_2$ primary alkaline battery with liquid KOH electrolyte has dominated the portable power market for nearly six decades [7].
- **Lithium primary batteries**. Since the beginning of primary battery research, many types of lithium primary batteries (LPBs) have begun to be implemented on a large scale [6].
- **Zinc-carbon batteries**. The zinc–carbon battery is the primary battery in the market due to its inexpensive raw materials, low internal resistance, high energy density and relatively stable discharge plateau [8].

### 2.1.2 Secondary Batteries

Unlike primary batteries, which are designed for a single use, secondary batteries offer the advantage of rechargeability, making them essential for modern applications requiring long-term, sustainable energy solutions. Secondary batteries are used as backup or temporary augmentation for another power source, such as in vehicles or laptop computers. They can also be used as the sole energy source instead of primary cells to reduce waste or avoid physically changing the battery when depleted.

A comprehensive understanding of secondary batteries requires analyzing the electrochemical and physical principles that govern their operation. These principles are described by fundamental equations that account for equilibrium potential, reaction kinetics, mass transport, and internal resistance [5]. The key governing equations for secondary batteries are as follows:

- **Equilibrium Voltage (Nernst Equation)**. The equilibrium potential of an electrode reaction is determined by the Nernst equation, which relates the cell voltage to the concentration of reactants and products:

$$E = E^o - \frac{RT}{zF} ln \frac{a_{products}}{a_{reactants}}$$

  where $E$ is the electrode potential, $E^o$ is the standard electrode potential, $R$ is the universal gas constant, $T$ is the temperature, $z$ is the number of transferred electrons, $F$ is Faraday's constant, and $a$ represents the species' activity [5].

- **Charge Transfer Kinetics (Butler-Volmer Equation)**. The rate of electrochemical reactions at the electrode interface is described by the Butler-Volmer equation:

$$i = i_o \left[ exp\left(\frac{\alpha_a z F \eta}{RT}\right) - exp\left(\frac{\alpha_c z F \eta}{RT}\right)\right]$$

  where $i$ is the current density, $i_o$ is the exchange current density, $\alpha_a$ and $\alpha_c$ are the anodic and cathodic charge transfer coefficients, and $\eta$ is the overpotential [5].

- **Mass Transport (Fick's Laws of Diffusion)**. One of the primary mechanisms of mass transport in electrochemical systems is diffusion, described by Fick's second law:

$$\frac{dC}{dt} = D\frac{d^2C}{dx^2}$$

  where $C$ is the concentration of species, $D$ is the diffusion coefficient, $t$ represents time, and $x$ is the spatial coordinate [5].

- **Ohm's Law (Internal Resistance Effects)**. The internal resistance of the battery leads to voltage loss, which is governed by Ohm's law:

$$V = IR$$

  where $V$ is the voltage drop, $I$ is the current, and $R$ is the internal resistance [5].

All batteries consist of a positive electrode, a negative electrode, and an ionic conductor (electrolyte). Many cells also have a separator that keeps the electrodes from short-circuiting but allows ions to flow. These components together form a cell and are schematically shown in Figure 2.1.

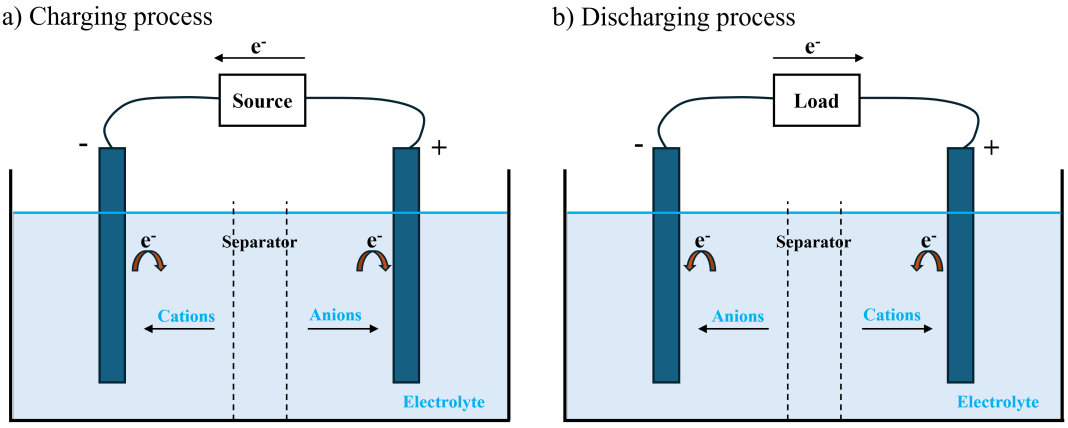


Figure 2.1: Basic battery operation for (a) charging and (b) discharging processes [9].

The operation of a cell during discharge is shown schematically in Figure 2.1.b. When the cell is connected to an external load, electrons flow from the anode, which is oxidized, through the external load to the cathode, where the electrons are accepted and the cathode material is reduced. The electric circuit is completed in the electrolyte by the flow of anions (negative ions) and cations (positive ions) to the anode and cathode, respectively [10].

During the recharge of a rechargeable or storage cell, the current flow is reversed and oxidation takes place at the positive electrode and reduction at the negative electrode, as shown in Figure 2.1.a. As the anode is, by definition, the electrode at which oxidation occurs and the cathode the one where reduction takes place, the positive electrode is now the anode and the negative the cathode [10].

As for primary batteries, there are different types of secondary batteries available today. The most widely used types of secondary batteries are the following ones.

- **Lead-acid batteries**. The lead-acid battery was developed by Raymond Louis Gaston Planté in 1860. This formed the basis for the first practical rechargeable battery. Despite other rechargeable batteries, the lead-acid battery is still very common in a wide range of applications. Because of their low energy density, lead-acid batteries are the choice when operating distance and weight are less important and a low price is crucial. Full power can be delivered by this type of battery extremely quickly. This makes them ideal for uses where a large amount of power may suddenly be needed, which is why they are used for electrically starting internal combustion engines in most vehicles [5] [9] [11].

  **Cathode reaction**: $\mathrm{PbO_2 + 3\,H^+ + HSO_4{}^- + 2\,e^-} \underset{\text{charging}}{\overset{\text{discharging}}{\rightleftharpoons}} \mathrm{PbSO_4 + 2\,H_2O}$

  **Anode reaction**: $\mathrm{Pb + HSO_4{}^-} \underset{\text{charging}}{\overset{\text{discharging}}{\rightleftharpoons}} \mathrm{PbSO_4 + H^+ + 2\,e^-}$

- **Nickel-metal hydride batteries**. Nickel-metal hydride (NiMH) batteries are, in some ways, similar to nickel-cadmium batteries, but they have some advantages including more power. In addition, memory effects can be reduced when quick charging is used. However, the batteries also must be frequently discharged or the memory effect may appear. Hydrides store hydrogen within their physical structure. The hydrogen can later be extracted to be used in the battery. A common hydride is an alloy based on nickel, aluminium, and rare earth metals though there is another based on titanium and zirconium. NiMH cells show the most promise for an aqueous electrolyte cell [5] [9].

  **Cathode reaction**: $\mathrm{NiO(OH) + H_2O + e^-} \underset{\text{charging}}{\overset{\text{discharging}}{\rightleftharpoons}} \mathrm{Ni(OH)_2 + OH^-}$

**Anode reaction**: $\mathrm{MH} + 2\,\mathrm{OH}^- \underset{\text{charging}}{\overset{\text{discharging}}{\rightleftharpoons}} \mathrm{M} + \mathrm{H_2O} + \mathrm{e}^-$

- **Nickel-cadmium batteries**. Nickel-cadmium (NiCd) batteries are widely used and still widely researched. They were invented by Waldemar Jungner in 1899. They are acceptable for high-temperature applications. These batteries are not used more often because of their high costs and the environmental concerns related to cadmium. They also have memory effects which cause a gradual reduction in capacity if they are not fully discharged and charged every cycle [5] [9].

  **Cathode reaction**: $2\,\mathrm{NiO(OH)} + 2\,\mathrm{H_2O} + 2\,\mathrm{e}^- \underset{\text{charging}}{\overset{\text{discharging}}{\rightleftharpoons}} 2\,\mathrm{Ni(OH)_2} + 2\,\mathrm{OH}^-$

  **Anode reaction**: $\mathrm{Cd} + 2\,\mathrm{OH}^- \underset{\text{charging}}{\overset{\text{discharging}}{\rightleftharpoons}} \mathrm{Cd(OH)_2} + 2\,\mathrm{e}^-$

- **Lithium-ion batteries**. The lithium-ion cell was invented in 1979 and provides an open circuit voltage of up to 4 V. Using lithium as an ion rather than as a metal solved the recharging problems due to dendrite growth. Still, the battery does not behave well if overcharged or heated and can lose capacity if either of these events occurs. Advantages include a relatively low self-discharge rate, no memory effect, lightweight, and high energy density [5] [9].

  **Cathode reaction**: $\mathrm{Li_{1-}}_x\mathrm{CoO_2} + \mathrm{xLi} + \mathrm{xe}^- \underset{\text{charging}}{\overset{\text{discharging}}{\rightleftharpoons}} \mathrm{LiCoO_2}$

  **Anode reaction**: $\mathrm{C}_y\mathrm{Li}_x \underset{\text{charging}}{\overset{\text{discharging}}{\rightleftharpoons}} \mathrm{C}_y + \mathrm{xLi}^+ + \mathrm{xe}^-$

Some technical details of these secondary battery technologies are summarized in Table 2.1 to provide a side-by-side comparison of some essential features.

Table 2.1: Comparison of key characteristic of rechargeable battery technologies [9] [12] [13].

| **Battery technology** | **Specific energy (Wh/kg)** | **Specific power (W/kg)** | **Cell voltage (V)** | **Cycle life (cycles)** | **Lifespan (years)** | **Max DoD (%)** | **Self-discharge rate (%/month)** |
|---|---|---|---|---|---|---|---|
| **Lead-Acid** | 30 - 50 | 180 - 400 | 2.1 | 500 - 1000 | 3 - 5 | 50 - 80 | 3 - 20 |
| **Nickel-Metal-Hydride** | 60 - 120 | 200 - 300 | 1.2 | 500 - 1000 | 5 - 7 | 60 - 80 | 20 - 30 |
| **Nickel-Cadmium** | 45 - 80 | 150 - 300 | 1.2 | 1000 - 2000 | 8 - 15 | 60 - 80 | 10 - 20 |
| **Lithium-Ion** | 100 - 265 | 250 - 1000 | 3.6 | 1000 - 5000+ | 8 - 15 | 100 | 2 - 8 |

The most promising technology is lithium-ion due to its high specific energy, specific power, and cell voltage. Furthermore, it is a unique technology that can achieve a 100% depth of discharge (DoD), and it has a low self-discharge. For these reasons, LiB technology is the primary energy source for electric vehicles.

## 2.2 Lithium-Ion Battery

### 2.2.1 LiB Operation

A lithium-ion cell usually consists of a metal oxide as the cathode, a mixture of organic carbonates containing a lithium-bearing salt as the electrolyte, and graphite as the anode. During charging, lithium ions ($Li^+$) move from the cathode through the electrolyte and intercalate into the anode, between the graphite layers; and, during discharge, they move in the reverse direction [14]. Figure 2.2 shows the charging and discharging processes of LiBs.

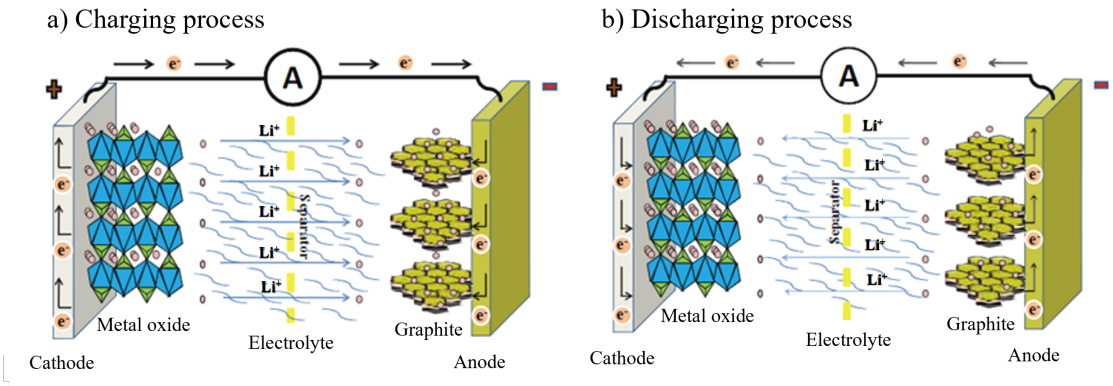


Figure 2.2: Typical LiB processes while (a) charging and (b) discharging [15].

### 2.2.2 Cathodes for LiBs

The comparison of key cathode materials (positive electrodes) used in LiBs is shown in Figure 2.3, highlighting their respective strengths and limitations, which are discussed below to identify the most suitable choice for EV applications.

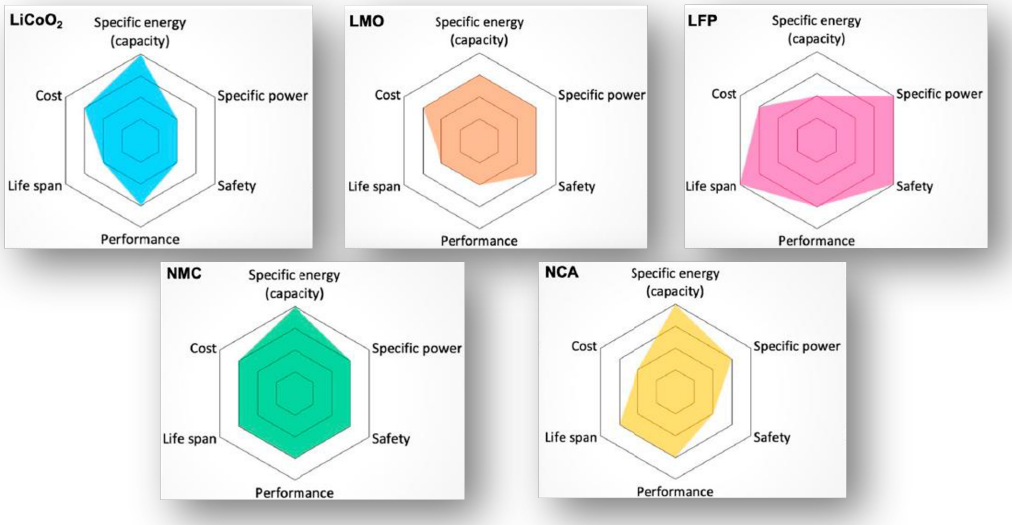


Figure 2.3: Comparison of today's cathode materials for LiBs [16].

Figure 2.3 graphically compares different types of LiBs used in EVs considering several characteristics. The major factors considered are specific energy, specific power, safety, performance, life span, and cost. Specific energy indicates the amount of energy a battery can store per unit weight,

which directly influences the driving range. Specific power is the ability to deliver high current on demand. Safety is naturally one of the most important aspects when choosing a battery for an EV. Performance reflects the battery's condition when driving the EV in extreme temperature conditions. Life Span reflects cycle count and longevity. Cost presents technology feasibility [17].

### Lithium Cobalt Oxide ($\mathbf{LiCoO_2}$)

Lithium Cobalt Oxide (LCO) batteries have been used in most personal electronics (laptops, cameras, tablets, etc.) due to their high energy density, long life cycle and ease of manufacturing. However, their reliance on cobalt presents significant challenges. Cobalt is a relatively scarce and costly material, which limits the economic viability of $LiCoO_2$ batteries for large-scale applications like EVs. Additionally, there are serious ethical concerns surrounding cobalt mining, particularly in regions like the Democratic Republic of the Congo, where child labor and unsafe working conditions have been widely reported. Despite these limitations, $LiCoO_2$ batteries have been used in early EV models such as the Tesla Roadster and the Smart Fortwo electric drive (ED) [17].

### Lithium Manganese Oxide ($\mathbf{LiMn_2O_4}$)

Lithium Manganese Oxide (LMO) batteries have low internal cell resistance which enables fast-charging and high-current discharging. This chemistry provides better thermal stability than the lithium cobalt oxide cathode but results in approximately 33% lower capacity and a lower life span due to high redox potential above 4.5 V, which cause electrolyte degradation in the cell [17].

### Lithium Iron Phosphate ($\mathbf{LiFePO_4}$)

Lithium Iron Phosphate (LFP) batteries offer good electrochemical performance with low resistance, besides high current rating and long cycle life. $LiFePO_4$ has a higher self-discharge compared to other LiB technologies, which can cause balancing issues with ageing. Further, moisture seems to significantly limit the lifetime of the battery [17].

### Lithium Nickel Manganese Cobalt Oxide ($\mathbf{Li(Ni_xMn_yCo_{1-x-y})O_2}$)

Lithium Nickel Manganese Cobalt Oxide (NMC) electrodes can be designed for high specific energy. The secret of NMC lies in combining nickel, manganese, and cobalt: nickel is known for its high specific energy but poor stability; manganese enhances structural stability but offers low specific energy; and cobalt improves electronic conductivity and thermal stability [18]. Researchers are using nickel-rich electrodes to increase energy density, while reducing the Co content is also helpful since it lowers costs. Companies have switched from NMC111 to NMC442 to NMC622, and now NMC811. Combining nickel and manganese enhances each other's strengths, making NMC the most successful Li-ion system suitable for EV powertrains. The current demand of these batteries is high given the high specific energy and excellent thermal characteristics. As mentioned above, NMC has been used by many EV manufacturers, including Nissan (Leaf) and BMW (i3) [17].

### Lithium Nickel Cobalt Aluminium Oxide ($\mathbf{Li(Ni_xCo_yAl_{1-x-y})O_2}$)

Lithium Nickel Cobalt Aluminium Oxide (NCA) shares similarities with NMC by offering high specific energy and specific power, and a long life span. NCA is not as safe as the others listed above and as such, requires special safety monitoring measures to be employed in EVs. They are also more costly to manufacture, which limits their viability in other applications [17].

Thus, among the presented state-of-the-art cathode materials, layered lithium nickel manganese cobalt oxide, $Li_yNi_{0.a}Mn_{0.b}Co_{0.c}O_2$ (NMCabc) is one of the most promising classes of cathode materials. Ni-rich compositions, where a $\geq 5$, are being widely explored [19].

Among other variants of NMCs, NMC811 possesses higher capacity, lower raw material cost, and lower global aggregate supply risk at the expense of reduced thermal stability and cycle life [20]. The high-energy-specific capacity and low Co content of NMC811 make it a promising material

for future high-energy-density LiBs. Cells containing NMC811 can achieve higher capacity density compared to those with lower Ni content NMCs (e.g., NMC532 or NMC622), which is interesting for EVs [21].

### 2.2.3 Anodes for LiBs

Another critical component of LiBs is the anode material, which significantly influences the battery's performance, longevity, and safety. Different anode materials for LiBs are categorized based on their lithiation mechanisms. Each type has distinct advantages and drawbacks, influencing its commercial viability [22]. Figure 2.4 gives the categorization of anode materials tested in LiBs.

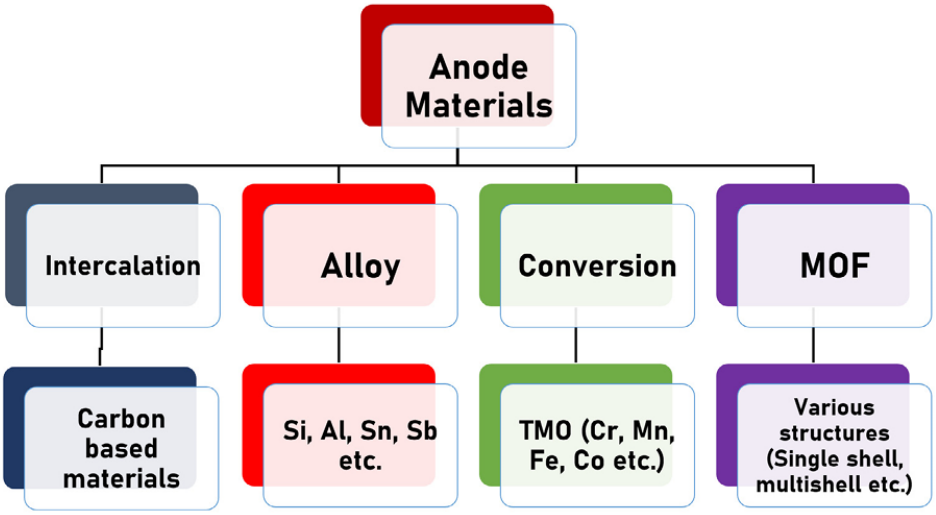


Figure 2.4: The different anode materials based on lithiation mechanism [22].

#### Intercalation Anodes

Intercalation anodes operate by reversibly inserting lithium ions into the host material's structure without causing significant phase changes. Two of the most widely studied intercalation-based anode materials for LiBs are graphite and lithium titanate ($Li_4Ti_5O_{12}$, or LTO).

**Graphite** is the most commonly used anode material in commercial LiBs due to its high structural stability, long cycle life, and compatibility with existing electrolytes. Carbon-based anodes can be categorized into soft and hard carbon, or more broadly into graphitic (crystalline) and non-graphitic (amorphous) forms. Non-graphitic carbon materials are known for their mechanical hardness. The lithium intercalation reaction in graphite can be described by the following equation [22]:

$$Li^+ + e^- + 6\,C \underset{\text{discharging}}{\overset{\text{charging}}{\rightleftharpoons}} LiC_6$$

Graphite's layered structure enables lithium-ion intercalation with minimal volume expansion (around 10%), which helps maintain mechanical integrity during cycling. Its low operating potential (approximately 0.3 V vs. $Li/Li^+$) makes it particularly efficient for energy storage. However, its relatively low theoretical capacity (372 mAh/g) limits the overall energy density of LiBs. Moreover, at high charge rates, graphite is prone to lithium plating, which can lead to dendrite formation and associated safety risks [22] [23].

**Lithium titanate** (LTO), on the other hand, offers superior safety and structural stability. It operates at a higher voltage plateau of approximately 1.55 V vs. $Li/Li^+$, which effectively eliminates the risk of lithium plating during fast charging, making it suitable for applications such as electric buses and stationary energy storage systems [24]. The lithiation reaction in LTO is:

$$\mathrm{Li_4Ti_5O_{12}} + 3\,\mathrm{Li^+} + 3\,\mathrm{e^-} \underset{\text{discharging}}{\overset{\text{charging}}{\rightleftharpoons}} \mathrm{Li_7Ti_5O_{12}}$$

LTO is often referred to as a "zero-strain" material due to its negligible volume change during cycling, which greatly enhances its cycle life. Despite these advantages, its lower specific capacity (approximately 175 mAh/g) and relatively poor electronic conductivity compared to graphite have limited its widespread adoption in mainstream electric vehicles [24].

### Alloy-Based Anodes (Silicon, Tin, Aluminium)

Alloy-based anodes like silicon, tin, and aluminium offer significantly higher lithium storage capacities, with silicon reaching an impressive 4200 mAh/g, more than ten times that of graphite. This high capacity has the potential to revolutionize LiB performance by drastically increasing energy density. However, these materials suffer from extreme volume expansion during lithiation, with silicon expanding up to 263%. This expansion leads to structural degradation, loss of electrical contact, and ultimately, poor cycle stability. Efforts to mitigate these issues, such as nanostructuring and carbon composites, show promise but have yet to achieve widespread commercial viability [22] [25].

The reaction for a silicon anode with lithium is as below [22]:

$$\mathrm{xLi^+} + \mathrm{Si} + \mathrm{xe^-} \underset{\text{discharging}}{\overset{\text{charging}}{\rightleftharpoons}} \mathrm{Li}_x\mathrm{Si}$$

### Conversion-Based Anodes (Transition Metal Oxides - TMOs)

Conversion-based anodes, which include transition metal oxides like $Fe_2O_3$, $Co_3O_4$, and $TiO_2$, offer an alternative with capacities exceeding graphite, typically ranging between 500–1000 mAh/g. These materials are abundant and relatively low-cost, and unlike graphite, they eliminate the risk of lithium dendrite formation. However, their poor electrical conductivity necessitates the use of conductive additives, and they undergo substantial volume changes during cycling, leading to electrode pulverization. Additionally, their low initial coulombic efficiency (CE) results in significant lithium loss in the first charge-discharge cycle, making them less practical for commercial applications without further improvements [22].

The reaction between TMO and lithium ions follows a conversion mechanism, as shown below [22]:

$$\mathrm{MO} + 2\,\mathrm{Li} + 2\,\mathrm{e^-} \underset{\text{discharging}}{\overset{\text{charging}}{\rightleftharpoons}} \mathrm{Li_2O} + \mathrm{M}$$

### Metal-Organic Frameworks (MOFs)

A more recent approach involves the use of MOFs as anode materials. These highly tunable porous structures can facilitate lithium storage via different lithiation mechanisms such as intercalation or conversion, depending on their specific composition. Their ability to accommodate volume changes could help enhance cycle life. Yet, their inherently low electrical conductivity remains a major challenge, often requiring additional conductive materials to make them viable for battery applications. While MOFs present an exciting research direction, they are still far from large-scale commercialization [22].

Ultimately, despite its limitations, graphite remains the dominant anode material due to its unparalleled combination of stability, efficiency, and manufacturability. While alternative materials promise higher capacities, they have yet to overcome critical issues such as volume expansion, structural degradation, and conductivity limitations.

## 2.3 Emerging Lithium-Based Battery Systems

LiBs remain the dominant technology for most applications, although advances are paving the way for alternatives with higher energy densities [26]. The most promising emerging technologies for the future are:

- **Solid-State Lithium Batteries**. Solid-state batteries are non-flammable, leak-proof, thermally stable, with no dendrites formed, etc. They enable the use of lithium metal's expanded energy density. Unlike liquid batteries in which electrolytes are liquid, solid-state batteries' components are in solid state.

  An electrolyte layer separates two electrodes in a solid-state electrolyte instead of a separator impregnated with a liquid electrolyte. The electrodes do not need to be separated by liquid or soft membranes when using solid electrolytes [26]. Figure 2.5 compares the conventional LiB and the all-solid-state lithium battery.

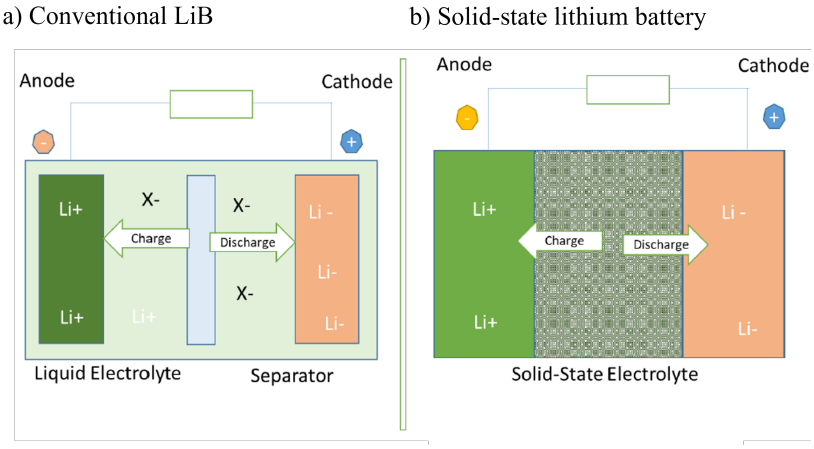


Figure 2.5: Structure of (a) LiB and (b) all-solid-state lithium battery [26].

- **Lithium-Sulfur Batteries**. For achieving energy densities above today's LiBs, metallic lithium is used as the active material at the anode. One of such systems is lithium-sulphur.

  The anode is metallic lithium and the cathode is a mix of elemental sulphur ($S_8$ rings) with carbon. Both, lithium and sulphur, are dissolved in the electrolyte and the lithium ions react with the polysulphides, which change their composition during the discharge. During the charge, these processes run the other way around. The carbon is needed for the conductivity to compensate for the low electrical conductivity of sulphur [11].

- **Lithium-Air Batteries**. Another approach to reach a high energy density is to use the atmosphere's oxygen as the active material on the cathode. This means that the anode is pure lithium oxidised with oxygen. Because oxygen is available everywhere, only the lithium metal has to be stored in the battery. Therefore the energy density increases dramatically owing to the low weight of the material stored in the battery. However, the battery weight increases during the discharge (and thus, the energy density decreases) because oxygen is incorporated as metal oxides.

  Between the lithium metal anode and the porous membrane, which is the contact with the atmosphere, there is an electrolyte which transports the dissolved lithium cations from the anode to the membrane where it reacts with the oxygen. Because of this membrane, this battery technology is a combination of the technologies of a battery and a fuel cell.

  However, besides the possible high energy density, there are still great challenges in lithium-air systems such as the number of cycles, the safety, and the lifetime [11].

## 2.4 Fast-Charging Batteries for EVs

### 2.4.1 Importance of Enabling Fast-Charging Capabilities

Fully battery-powered electric vehicles have become one of the most popular classes of green vehicles. Among all the factors against the widespread adoption of EVs, the relatively long charging time is arguably one of the most difficult limitations for consumers to accept and for researchers to meet [27].

Achieving battery charging performance comparable to the current refueling experience of gasoline vehicles is essential for further penetration into the mass vehicle market. Therefore, enabling a fast-charge experience can catalyze substantial BEV adoption [28].

The battery charging rate is usually indicated in a unit known as the C-rate. The C-rate normalizes the absolute current with the capacity of the active material, resulting in a set time interval during which the cell is expected to be fully charged or discharged. A 1C rate corresponds to a complete charging time of 1 hour, while a 2C rate means charging is completed in 30 minutes.

In practice, the complete charging protocol of EVs is never a constant current but usually switches to a constant voltage protocol nearing full charge to prevent side reactions. Therefore, a commercial EV undergoing fast charging will experience a high C-rate (around 2C) until reaching 80% SOC, followed by a slower and gentler constant voltage phase to achieve full charge [27].

Currently, the shortest recharging time for a LiB pack in electric vehicles is on the order of 30 min (2C rate) to achieve an 80% state of charge (SOC), while filling up a gasoline car's tank from 0% to 100% typically takes between 2 to 5 minutes. Thus, decreasing the charging time of EVs to 15 min or less has been viewed as one of the most essential factors for the widespread adoption of EVs in the marketplace. As a result, a global effort is underway to enable fast-charging capabilities for LiBs by engineering them to safely tolerate rates of 6C or greater, i.e., charging times of 10 min or less [19].

### 2.4.2 Problems Associated with Fast Charging

Higher charging rates can negatively impact battery performance, safety, and lifespan, leading to issues such as lithium plating, accelerated side reactions, and elevated temperatures [14].

Most fast-charge studies have focused on the Li-plating constraints at the anode, and relatively less focus has been given to cathode ageing. In the short term, the cathode can dominate cell polarization, and therefore, can limit charge acceptance under fast-charging conditions. Improving cathode beginning-of-life performance by developing novel cathode chemistries, cathode compositions, and optimizing electrode design is a crucial need to enable fast charging [28].

At high $Li^+$ extraction rates, the volume changes experienced by the cathode particles are further amplified, increasing heterogeneity compared to that of slower rates, and creating more stress throughout the battery material. This is because the Li-ion diffusion-induced stress is amplified at higher currents, such as in fast-charging conditions. Surface cathode primary particles tend to have a higher SOC than the inner primary particles. Cracking of the cathode material might reduce accessible Li storage sites in addition to generating more surface area for electrolyte decomposition [27].

To mitigate these challenges, optimizing cathode properties plays a crucial role in improving the fast-charging capabilities of LiBs.

### 2.4.3 Cathode Properties for Fast Charging

Some researchers have studied the fast-charging behaviour of the NMC cathode. For example, Yang et al. used single-layer pouch (SLP) cells to compare two electrode loadings: low-loading (1.5 $mAh/cm^2$) and high-loading (2.5 $mAh/cm^2$), and three cathode materials: NMC532, NMC622 and NMC811. For both loadings, noticeably better performance was observed in the NMC811

cells, and the obtained results suggest that the high Ni content in NMC811 enables the high rate capability through improved electronic conductivity and $Li^+$ diffusivity [19].

The same research also reported that the coulombic efficiency, the charge capacity, as well as the discharge capacity are higher for the low-loading compared to the high-loading cathodes. This brings us information about better performance under fast-charging conditions for low-loading electrodes (thinner electrodes). However, using thinner electrodes also requires more cells to achieve the same energy density, leading to an increase in the cell nonactive materials [19].

In addition to NMC-based cathodes, other chemistries such as LFP and LCO have also been evaluated for their fast-charging capabilities. LFP exhibits strong thermal stability and structural robustness, enabling it to support high-rate charging up to 5C with minimal degradation, as reported by Wu et al. [29]. This is attributed to its stable olivine structure and fast lithium-ion diffusion. Nevertheless, LFP's lower intrinsic electronic conductivity often requires conductive coatings or particle downsizing to ensure optimal performance. In contrast, LCO delivers higher energy density but suffers from reduced structural and thermal stability at high C-rates, which limits its effectiveness in fast-charging applications. These trade-offs highlight the importance of selecting cathode materials based on the specific demands of power, energy, and safety [29].

### 2.4.4 Fast-Charging Protocols

In addition to the developments of advanced electrolytes, active materials, and electrodes, the fast-charging capability of LiBs can be improved by using optimized the charging protocol [30]. There are some protocols that help minimize the temperature increase inside a battery, the lithium plating, and its charging time [31].

Different charging–discharging strategies can help minimize battery degradation. One such strategy is multistage constant current–constant voltage (MCC-CV), which determines the current level in stages based on the state-of-charge (SOC) range. Another approach is pulse charging, where the cell is periodically charged using pulse currents separated by defined rest or discharge intervals [30] [31].

## 2.5 X-Ray Diffraction for Li-ion Battery Research

Achieving fast-charging capabilities without compromising battery performance or lifespan remains one of the most critical challenges in battery development. This requires a thorough understanding of how materials behave under high-rate cycling conditions, particularly in terms of structural stability and degradation mechanisms. XRD provides valuable insights in this context by enabling the analysis of phase transitions, structural evolution, and lattice changes occurring during repeated charge–discharge cycles. These insights are essential for identifying material limitations and guiding the design of electrode compositions that can better withstand the mechanical and electrochemical stresses imposed by fast charging [32].

XRD is based on the scattering of X-rays by the atoms in a crystalline structure, producing a diffraction pattern that provides information on the atomic arrangement and unit cell parameters. In battery materials, XRD is widely used to study unit cell expansion and contraction during lithium-ion intercalation/deintercalation, phase transformations, and potential structural degradation [32].

Thanks to the highly ordered crystal structure of the NMC811 cathode, structural changes can be easily detected using XRD. NMC811 has a layered rhombohedral crystal structure of the $\alpha$-$NaFeO_2$-type with R-3m symmetry, where transition metals are distributed within the oxide lattice (Figure 2.6) [33].

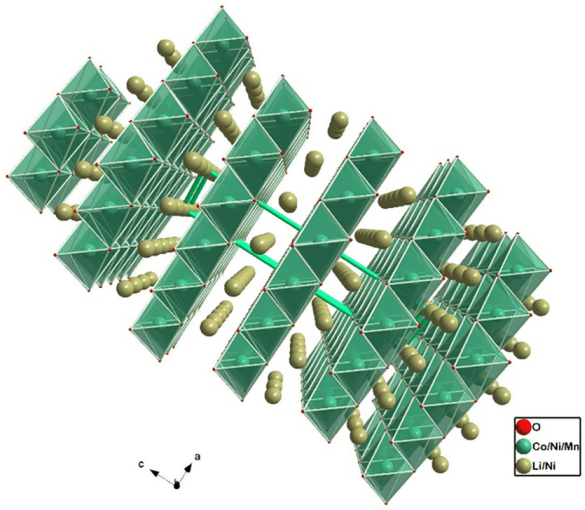


Figure 2.6: Rhombohedral (layered) structure for NMC811. Space group: R-3m [34].

To improve spatial and temporal resolution in battery materials studies, advanced XRD techniques have been developed, including in-situ and operando XRD. While ex-situ analysis involves removing the electrodes from the cell after cycling for characterization, in-situ and operando techniques allow real-time monitoring of structural evolution under actual operating conditions. In-situ XRD refers to the characterization of a material within the battery without disassembly, whereas operando XRD is performed while the cell is operating under electrochemical control [32].

Recent studies have demonstrated that high-energy synchrotron XRD is particularly useful for analyzing structural transformations of the NMC811 cathode in LiBs during aging. Synchrotron experiments have shown that NMC811 degradation is not primarily caused by significant bulk structural changes but rather by the formation of a resistive surface layer, which contributes to increased impedance and capacity loss over cycling [33].

Operando XRD studies have also established a correlation between unit cell parameter variations and capacity fading in NMC811|graphite full cells after extensive cycling. XRD analysis has revealed the presence of microstructural strain and intergranular cracking in nickel-rich materials, which contribute to their degradation [33]. These findings highlight the importance of advanced characterization techniques for understanding degradation mechanisms and optimizing LiB performance.

Friedrich et al. studied this highly crystalline structure using XRD, and Figure 2.7 shows the diffractogram they obtained from fresh NMC811 powder [33].

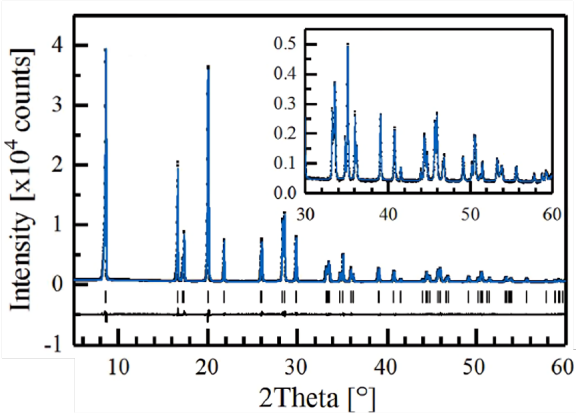


Figure 2.7: Diffractogram obtained by Friedrich et al. of NMC811 powder [33].

## 2.6 Scope of the Thesis

This project aims to optimize cathode composition and loading to enable fast-charging capabilities in LiBs, focusing on improving the cathode's performance and longevity under high C-rate conditions. Specifically, this research addresses the critical trade-off between fast-charging capability and battery lifespan, which is a major hurdle for the widespread adoption of EVs.

By examining a range of cathode compositions based on NMC811, this study investigates the interplay between material properties and electrode architecture to identify configurations that minimize degradation during high-rate charging. Additionally, various coating thicknesses are explored to balance areal capacity and mechanical stability, two of the key factors influencing charge acceptance and efficiency. The research encompasses both, experimental testing and electrochemical characterization, allowing for a comprehensive evaluation of performance metrics.

The outcomes of this thesis are expected to contribute to advancing battery technology by providing insights into optimizing electrode design for fast-charging applications. This work aligns with the broader goal of enabling a sustainable energy transition, addressing both consumer needs for quicker charging and the environmental imperative of reducing fossil fuel dependency.

# Chapter 3

# Materials and Methods

## 3.1 Cathode Fabrication

The cathodes were prepared inside a dry room with a dew point of -60 °C. NMC811 powder (MTI Corporation) was used as the cathode active material (CAM), polyvinylidene fluoride (PVDF, Alfa Aesar) as the binder, and Timical Super C65 (CB, MTI Corporation) as the conductive agent. The mixing process began by dissolving the binder in N-methyl-2-pyrrolidone (NMP, VWR), which acts as the solvent. Once fully dissolved, the conductive agent and active material were added to the solution, resulting in a homogeneous black slurry. The solid-to-liquid ratio of the slurry was maintained at 40%, ensuring optimal viscosity and coatability during electrode fabrication. This study investigated cathodes with varying proportions of NMC811, CB, and PVDF, as detailed in Table 3.1. The prepared slurry was then coated onto an aluminium foil, which serves as the cathode current collector. Two different wet coating thicknesses were applied to produce electrodes with different loadings, summarized in Table 3.2.

Table 3.1: Initial cathode compositions (wt%).

| **NMC811** | **CB** | **PVDF** |
|---|---|---|
| 85 | 5 | 10 |
| 88 | 5 | 7 |
| 90 | 5 | 5 |
| 90 | 3 | 7 |
| 90 | 7 | 3 |

Table 3.2: Thicknesses for each loading.

| **Loading** | **Wet thickness** ($\mu m$) |
|---|---|
| Low loading | 300 |
| High loading | 400 |

A vacuum oven is then used to remove the solvent at 90 °C, followed by a rolling procedure at 60 °C to remove any porous part. Figure 3.1 shows the MSK-HRP-1A Hot Rolling Press used for the rolling process.

Figure 3.1: MSK-HRP-1A Hot Rolling Press.

### 3.1.1 Coin Cell Cathode

Once dried and rolled, the cathode was cut into 15 mm diameter circular pieces. This is the size and shape necessary to fit inside the 2032 coin cell.

A punching machine was used to cut the cathode, which was wrapped in oven paper to prevent material damage. Once all the circular cathode pieces were collected in a vial, they were transferred into the glovebox for cell assembly. Figure 3.2 illustrates the punching machine used for cutting and the cathode disc after the process.

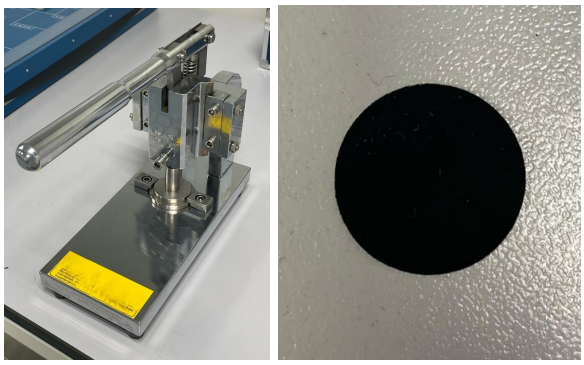

Figure 3.2: Punching machine used for cutting and cathode disc after the process necessary for the coin cell.

### 3.1.2 Pouch Cell Cathode

After the drying and rolling processes, the cathode was cut using the MSK-180-S Electrode Punching Machine. Figure 3.3 shows the punching machine used for cutting, along with the cathode in its final rectangular shape after the process.

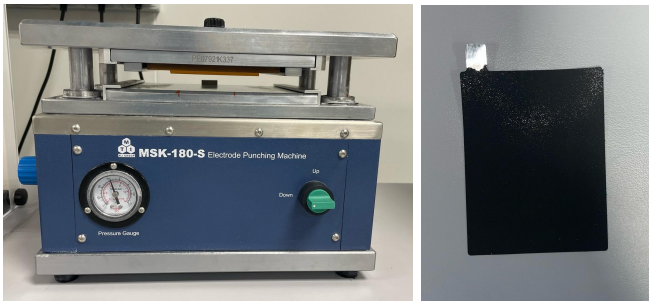


Figure 3.3: Punching machine used for cutting and cathode in its final shape after the process necessary for the pouch cell.

## 3.2 Cell Assembly

Two different types of cells were assembled and tested in this work: coin half-cells and pouch full-cells.

### 3.2.1 Coin Half-Cells

To better analyze the performance of one specific electrode material without the interference of the other electrode, lithium-ion half-cells are often used. In this work, half-cells were used to study the cathode's performance. The prepared cathode under study was the working electrode and it was assembled with a well-known and stable reference electrode as lithium metal.

The coin cells were used to make half-cells because it gives the possibility of using metal lithium. Using metal lithium in pouch cells would be inefficient due to the high amount of lithium we would need, and dangerous due to the possible reaction between lithium and water or oxygen.

Since lithium metal easily reacts with oxygen, it must be handled in an inert atmosphere. Figure 3.4 shows the glovebox filled with argon used to assemble the coin half-cells.

Figure 3.4: Glovebox used in this work.

Each half-cell consists of a 1.77 $cm^2$ NMC811 cathode (section 3.1.1) placed on an aluminium current collector and a 1.77 $cm^2$ lithium plate positioned on a stainless steel spacer. These components were separated by a Celgard 3501 monolayer microporous polypropylene (PP) membrane and soaked with 80 µL of 1.0 M $LiPF_6$ in a 50:50 (v/v) ethylene carbonate (EC)/dimethyl carbonate (DMC) electrolyte. Additionally, a second stainless steel spacer and a spring were incorporated, forming a non-pressurized coin half-cell.

To create a pressurized coin half-cell, an additional spring was introduced. This ensures that the cell remains under pressure, as the total thickness of the internal components is 3.2 mm (spring: 1 mm; spacer: 0.5 mm; electrodes + separator: 0.2 mm), while the available internal gap is only 3 mm. Figure 3.5 displays an image of the individual components before assembly inside the glovebox.

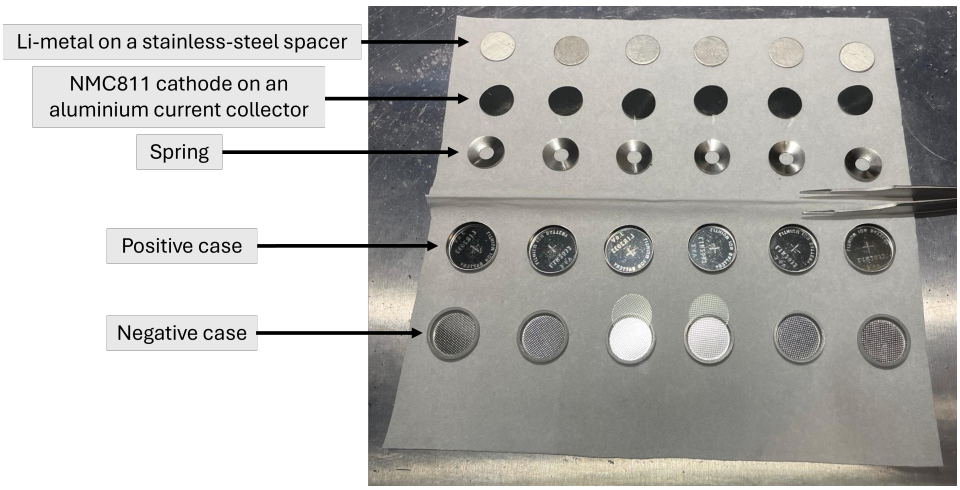


Figure 3.5: Different parts of the coin half-cell before assembling inside the glovebox.

In addition, Figure 3.6 shows schematically how the different parts were placed inside the coin cell for the non-pressurized (Figure 3.6.a) and the pressurized (Figure 3.6.b) cells.

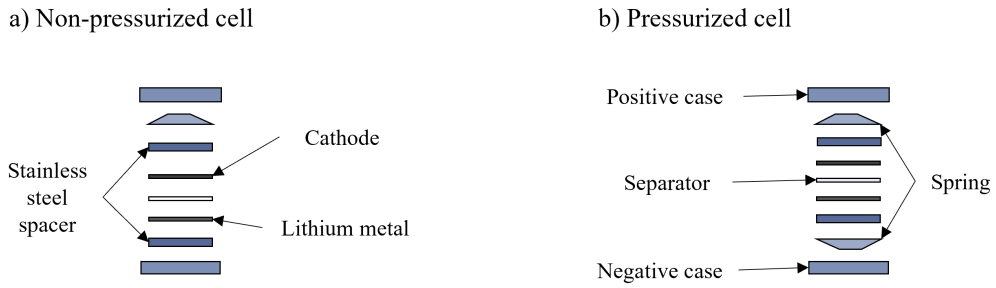


Figure 3.6: Scheme showing the order of the different parts in the coin half-cell for (a) non-pressurized and (b) pressurized cells.

### 3.2.2 Pouch Full-Cells

Pouch full-cells featuring graphite anodes were employed in order to evaluate more accurately the fast-charging performance of the cells under realistic conditions. Copper served as the anode current collector. The graphitic anodes were precisely shaped using the MSK-180-S Electrode Punching Machine (Figure 3.3) with a 45 mm × 58 mm template, while the cathodes were cut using a 43 mm × 56 mm template. The separator used in the pouch cells has slightly larger dimensions to ensure complete coverage and avoid short circuits: its height is slightly greater than that of the electrodes, and its length is approximately twice as long, as can be seen in the schematic representation in Figure 3.7.

In lithium-ion cells, the typical ratio of the negative (anode) to positive (cathode) electrode capacity (N/P) is usually around 1.1 to 1.2. This means that the anode capacity is slightly larger than the cathode capacity. This ratio helps ensure that the anode can accommodate all the lithium ions that migrate during charging, preventing issues like lithium plating on the anode during fast charging, which can be detrimental to the cell's performance and safety.

To assemble the pouch cells, Kapton tape, a polyimide film known for its excellent thermal and electrical insulation properties, was used to secure the different internal components in place. Additionally, an aluminium tab was attached to the aluminium part extending from the pouch cell, which is part of the cathode current collector; while a nickel tab was affixed to the copper part extending from the pouch cell, corresponding to the anode current collector. These metal strips facilitate reliable electrical connections and improve the overall conductivity of the cell.

In this case, the entire assembly process took place in the dry room as no metallic lithium was used. The pouch full-cells consist of single-layer cells, using the same separator as for the coin half-cells. Figure 3.7 provides a schematic representation of the electrodes, current collectors, and separator arrangement.

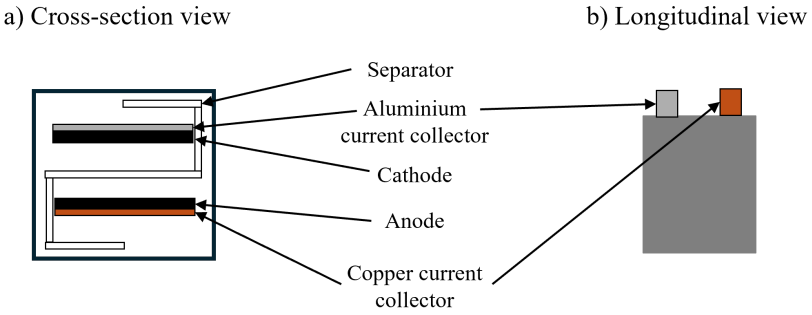


Figure 3.7: Scheme showing the order of the different parts in the pouch full-cell from (a) the cross-section view and (b) the top view.

Following the electrodes and separator assembly, the components were placed inside a pouch, and the electrolyte was added. The electrolyte composition was identical to that used in the coin half-cells, adding 20 µL per $cm^2$ of anode, resulting in a total volume of 0.52 mL. After electrolyte addition, the pouch cell was sealed using the Audionvac VMS 43 equipment (Figure 3.8).


Figure 3.8: Device used for sealing the pouch cells (Audionvac VMS 43).

## 3.3 Characterization Techniques

Different characterization techniques were used in this work and they are described below.

### 3.3.1 Electrochemical Testing

The electrochemical performance was evaluated using techniques such as galvanostatic cycling and electrochemical impedance spectroscopy (EIS), employing a high-precision potentiostat/galvanostat (BioLogic-BCS) and battery cyclers (Neware BTS 5V10mA). This equipment has been used to perform C-rate analysis and long-term cycling tests. Both NMC811/Li coin half-cells and NMC811/graphite pouch full-cells were electrochemically tested.

#### C-rate Analysis Conditions:

Galvanostatic cycling tests were performed at room temperature (20 ± 2 °C) using Neware or BioLogic equipment to analyse the different cathodes. BioLogic allows for higher currents than Neware (above its 1 A limit) and enables EIS measurements, which Neware does not support.

A C-rate test was conducted, with charge/discharge rates of 0.1C, 0.2C, 0.33C, 0.5C, 1C, and 2C, assuming an NMC811 specific capacity of 200 mAh/g. All the electrochemical potentials in this half-cell study are referenced to $Li/Li^+$.

#### Long-Term Cycling under Fast-Charging Conditions:

The cycling protocol involves galvanostatic charging at a 2C rate and discharging at a 0.33C rate. This approach minimizes degradation during discharge, allowing for a focused evaluation of the charging process.

The testing protocol consists of several steps: i) EIS measurement, ii) charging and discharging at 0.1C for three cycles to activate the cell and form the Solid-Electrolyte Interphase (SEI), iii) EIS measurement, iv) long-term fast charging at 2C and discharging at 0.33C for 200 cycles, v) EIS measurement, vi) charging and discharging at 0.1C for 3 cycles.

The EIS measurements were conducted over a frequency range spanning from 10 kHz to 0.1 Hz, allowing for the characterization of both charge transfer and diffusion-related processes.

The voltage window for all electrochemical tests was set between a lower cut-off potential of 2.8 V and an upper cut-off potential of 4.2 V. This range was selected to strike a balance between capacity utilization and cell stability, enabling a representative assessment of performance while minimizing excessive degradation. For each cathode composition and loading condition, three identical cells were tested to evaluate reproducibility. Among them, the cell exhibiting the most consistent and reliable performance was selected for detailed analysis.

### 3.3.2 X-Ray Diffraction (XRD)

XRD is used in this dissertation to study the changes in crystal structure and phases present in the cathode material. The XRD equipment used is the Malvern Panalytical-Empryean (Figure 3.9).

Figure 3.9: Malvern Panalytical-Empryean XRD equipment.

XRD analysis was performed at room temperature (20 ± 2 °C) using Mo-$K_{\alpha 1}$ radiation (0.7093 Å, 60 kV, 40 mA) over a $2\theta$ range of 5–50°.

The end-of-the-test (EOT) and intermediate state of charge (SOC) cathodes were obtained by disassembling the coin cells (ex-situ XRD). The electrodes were rinsed with dimethyl carbonate (DMC) to remove any residual electrolyte before the XRD measurement.

# Chapter 4

# Results and Discussion

## 4.1 Coin Half-Cell Performance

### 4.1.1 C-rate Study

#### a) Cathode Composition Analysis

Various cathode compositions (NMC811/CB/PVDF, wt%) were tested at different C-rates using coin half-cells: 85/5/10, 88/5/7, 90/5/5, 90/3/7, and 90/7/3 (Table 3.1). The results indicate that using the non-pressurized cells (one spring (1S)), only the 85/5/10 cathode composition could sustain the high charging rate (2C), as shown in Figure 4.1. The performance of different cathode compositions was evaluated using low-loading cathodes (300 µm wet thickness; ∼60 µm dry thickness). The wet thickness is always presented to indicate the loading used in each graph.

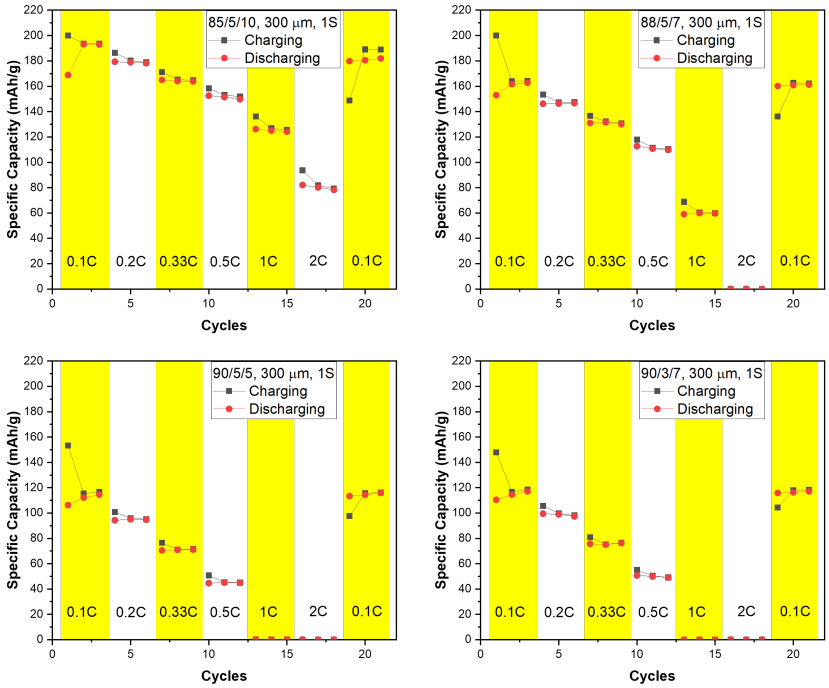


Figure 4.1: Specific capacity of the different cathode compositions at different C-rates. Low-loading and non-pressurized cells.

Due to its low polymer binder (PVDF) content, the 90/7/3 cathode lacked mechanical integrity and was too brittle for coin cell assembly. Additionally, the 90/5/5 cathode also began to exhibit signs of brittleness, indicating that using less than 5 wt% of polymer binder compromises the structural stability of the cathode, making it unsuitable for practical use. Figure 4.2 shows the detachment of the 90/7/3 cathode from the aluminium current collector, illustrating this issue.

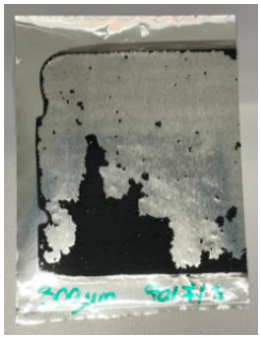

Figure 4.2: Brittleness of the 90/7/3 low-loading cathode.

To evaluate potential performance improvements, an extra spring was added to put the cell under pressure, thereby improving contact between components inside the coin cell (Figure 3.6.b). The results demonstrated enhanced performance, suggesting that this additional pressure contributed to improving fast-charging capabilities. Figure 4.3 presents the capacity at different C-rates using the pressurized cells (two springs (2S)). As before, just the low-loading cells are shown for this comparison.

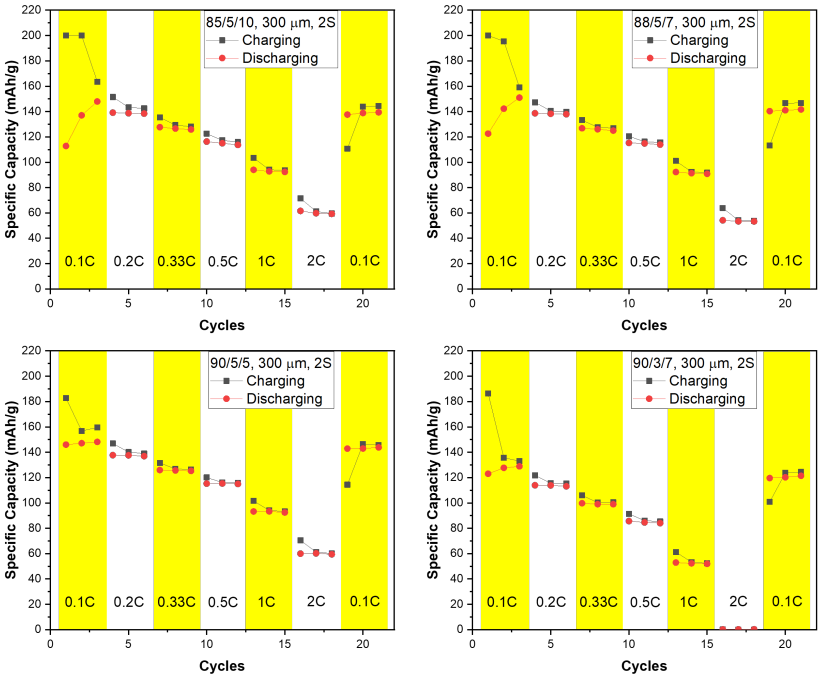


Figure 4.3: Specific capacity of the different cathode compositions at different C-rates. Low-loading and pressurized cells.

This improvement suggests that better mechanical contact enhances electrical conductivity within the cell, reducing the internal resistance associated with charge transfer and lithium-ion diffusion. This effect can be analyzed through EIS measurements. Figure 4.4 presents the Nyquist plots obtained from the coin half-cells with the 90/5/5 cathode, comparing the non-pressurized and the

pressurized cells after C-rate testing. This cathode composition was chosen for resistance analysis as it demonstrated the most significant improvement when a second spring was added.

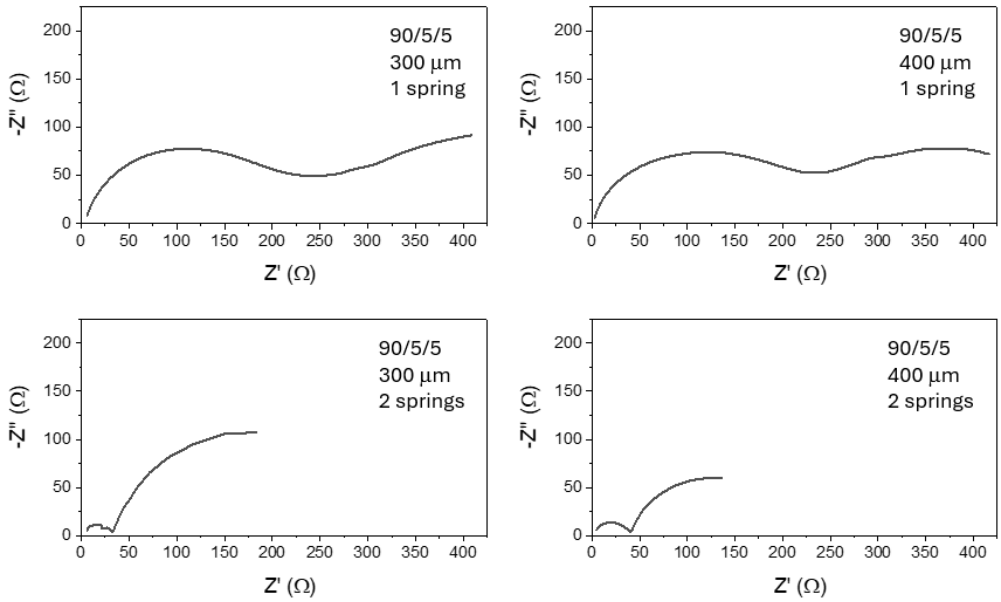


Figure 4.4: Nyquist plots to compare the internal resistance between non-pressurized and pressurized cells for the 90/5/5 cathode composition.

The high-frequency semicircle in Figure 4.4 is related to the charge transfer resistance. At the same time, the low-frequency linear region represents the Warburg impedance, which is associated with lithium-ion diffusion within the electrodes [35]. These EIS measurements were analyzed using the Equivalent Electric Circuit (EEC) methodology:

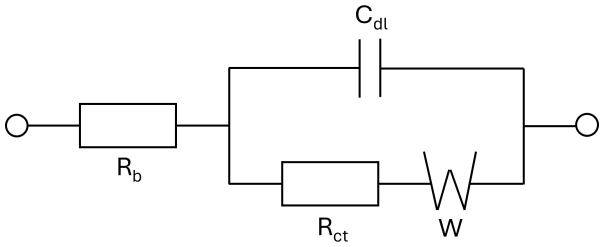


Figure 4.5: Equivalent Electric Circuit to the Nyquist plots.

This EEC includes different components: $R_b$ is the resistance of the cell's bulk; $C_{dl}$ is the double layer's capacitance; $R_{ct}$ is the charge transfer resistance; and $W$ is the Warburg impedance. The experimental EIS spectra were fitted to this EEC. Table 4.1 shows the values of these parameters for this 90/5/5 cathode composition for the two different loadings and pressurized and non-pressurized cells.

Table 4.1: Comparison of the charge transfer resistance, the Warburg impedance, and capacitance effect for each half-cell using the 90/5/5 cathode.

| **Cell configuration** | $\mathbf{R_{ct}}$ $(\Omega)$ | $\mathbf{W}$ $(\Omega/\sqrt{s})$ | $\mathbf{C_{dl}}$ $(\mu F)$ |
|---|---|---|---|
| 300 µm, non-pressurized | 188.1 | 161.2 | 2.9 |
| 300 µm, pressurized | 21.2 | 89.6 | 3.2 |
| 400 µm, non-pressurized | 174.9 | 176.3 | 3.7 |
| 400 µm, pressurized | 29.4 | 63.3 | 3.0 |

By analyzing the data presented in Table 4.1, it becomes evident that the addition of the second spring leads to a noticeable reduction in both, the charge transfer resistance and the Warburg impedance. This reduction indicates an enhancement in the electrochemical kinetics, thereby facilitating the cell's ability to operate under fast-charging conditions. Furthermore, the double-layer capacitance remains unchanged, suggesting that the electrode/electrolyte interface is not significantly affected by the modification.

These findings imply that the second spring effectively improves ion transport and reaction kinetics without compromising interfacial stability. Therefore, incorporating such mechanical adjustments could be a promising strategy for optimizing cell performance under high-rate charging scenarios.

On the other hand, when comparing the C-rate test results for the 85/5/10 cathode composition between pressurized and non-pressurized cells, the performance appears to be nearly identical. To investigate the reason behind this behaviour, Figure 4.6 presents the Nyquist plots for both loadings, comparing pressurized and non-pressurized cells.

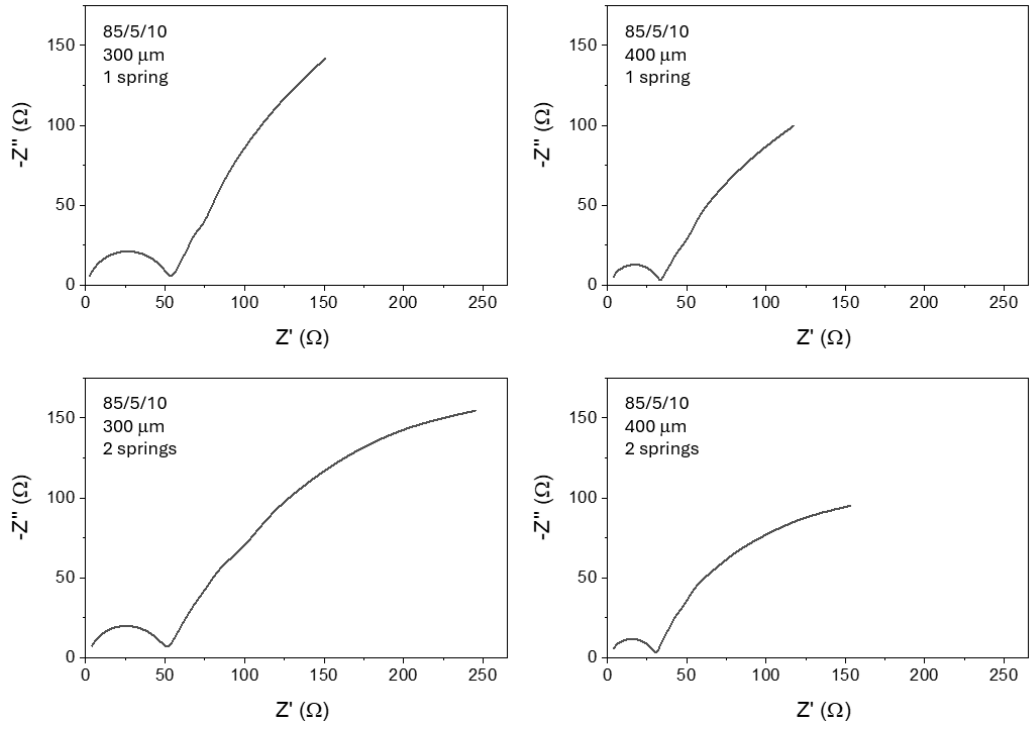


Figure 4.6: Nyquist plots to compare the internal resistance between non-pressurized and pressurized cells for the 85/5/10 cathode.

To better compare the results, Table 4.2 shows the parameters' value adjusted to the same EEC as in the previous case.

Table 4.2: Comparison of the charge transfer resistance, the Warburg impedance, and capacitance effect for each half-cell using the 85/5/10 cathode.

| **Cell configuration** | $\mathbf{R_{ct}}$ **(Ω)** | **W** $(\Omega/\sqrt{s})$ | $\mathbf{C_{dl}}$ $(\mu F)$ |
|---|---|---|---|
| 300 µm, non-pressurized | 44.5 | 91.3 | 2.9 |
| 300 µm, pressurized | 20.1 | 110 | 3.1 |
| 400 µm, non-pressurized | 25.3 | 61.9 | 3.1 |
| 400 µm, pressurized | 22.8 | 75.3 | 2.7 |

When comparing pressurized and non-pressurized cells at the same loading for the 85/5/10 cathode composition, the values are very similar, confirming the observation from the C-rate tests that their behaviour is nearly identical.

Moreover, as shown in Figures 4.1 and 4.3, the 90/3/7 cathode composition could not sustain a 2C charge rate even under pressure. This indicates that mechanical improvements alone are insufficient and highlights the critical role of the cathode's conductive material in enabling fast-charging capabilities. Specifically, the active material-to-carbon black ratio for this cathode composition is 30, whereas, in the other three studied compositions, this ratio ranges between 17 and 18. The higher ratio in the 90/3/7 cathode suggests that its carbon black content is insufficient to effectively facilitate electron transport, reinforcing the need for an increased carbon black fraction to support fast-charging capabilities.

Given that the 85/5/10 cathode exhibited the best high-rate performance with an active material-to-carbon black ratio of 17, additional cathodes were fabricated with the same ratio but a higher active material content: 88/5.18/6.82 and 90/5.3/4.7. Since the active material is the primary contributor to capacity, our goal was to maximize its content while maintaining the ability to sustain fast-charging rates and ensuring sufficient mechanical integrity. The results confirmed that a minimum of 5 wt% of PVDF is necessary, as the 90/5.3/4.7 cathode was too brittle for testing. The 88/5.18/6.82 cathode's performance is shown in Figure 4.7, where it can be observed that it could support the fast-charging conditions in all the cases except high-loading with the non-pressurized cell.

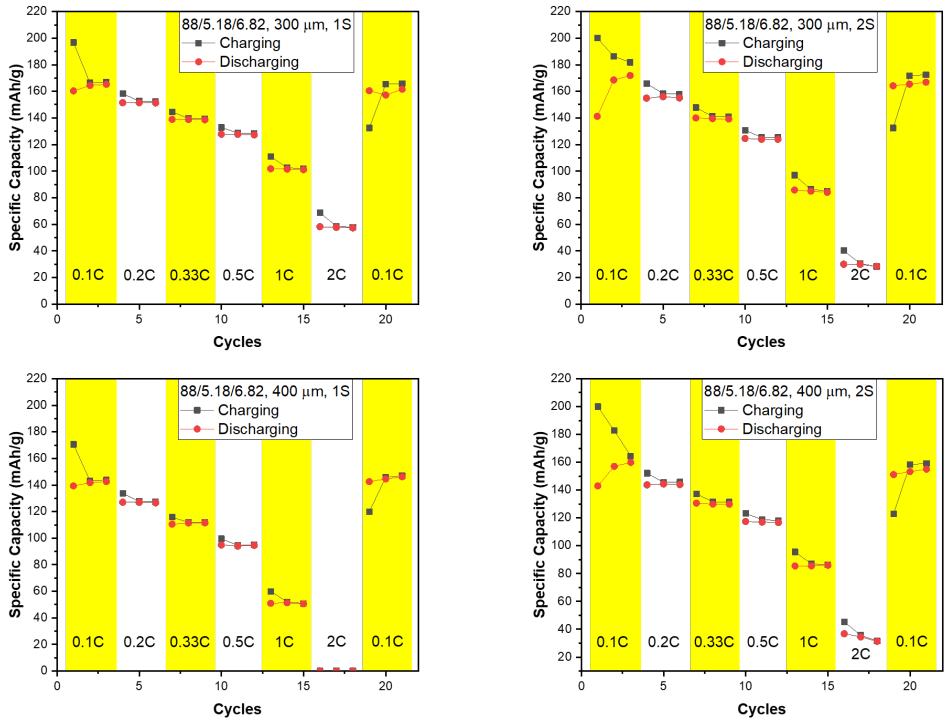


Figure 4.7: C-rate testing of the 88/5.18/6.82 cathode for the two different loadings and non-pressurized and pressurized cells.

### b) Cathode Loading Analysis

This section analyzes the effect of cathode loading by comparing the two wet thicknesses: 300 µm and 400 µm. By evaluating their electrochemical performance under different C-rates, the impact of increased loading on fast-charging capability can be assessed. This comparison provides insights into how electrode loading influences the overall behaviour of the cells, particularly in high-rate conditions.

Figure 4.8 presents the specific capacity at different C-rates for each cathode composition, focusing on the results obtained with the pressurized cells. Only these results are shown since the additional spring allowed the cells to sustain fast-charging conditions. As previously discussed, the 90/3/7 composition is excluded because it could not support fast-charging conditions. The figure is structured to compare low and high cathode loadings: the first row displays data for the low-loading cathodes, while the second row corresponds to the high-loading cathodes. The theoretical specific capacity for each composition and loading is also included to further aid interpretation.

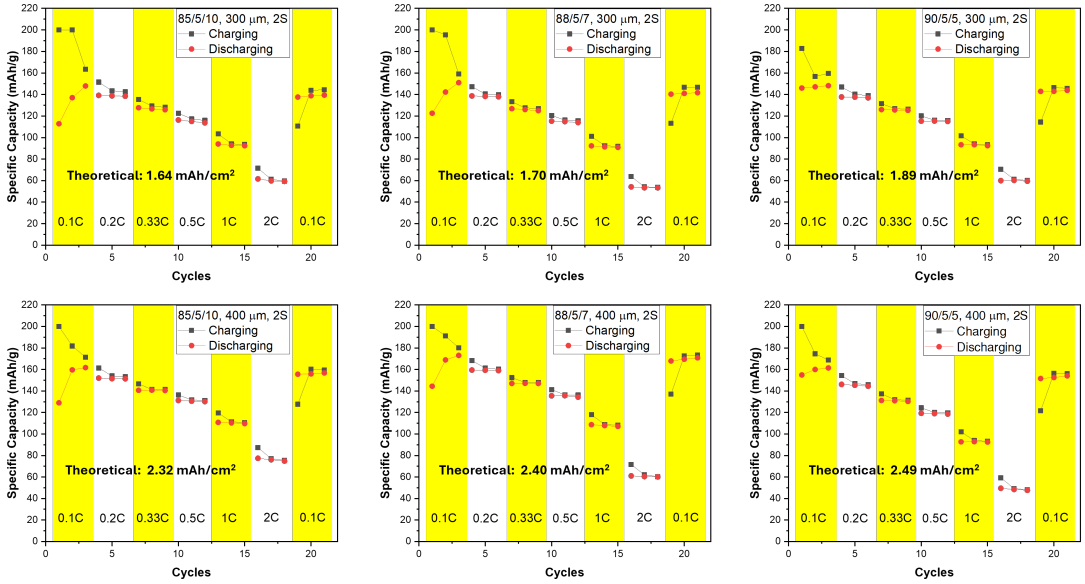


Figure 4.8: Specific capacity at different C-rates for low and high loading cathodes, using the pressurized cells.

By examining the C-rate testing shown in Figure 4.8, it is challenging to determine which loading best supports fast-charging conditions. However, the C-rate analysis of the 88/5.18/6.82 cathode (Figure 4.7) indicates that lower loading tends to result in improved cell performance.

### 4.1.2 Long-Term Cycling under Fast-Charging Conditions

#### a) Cathode Composition Analysis

A long-term cycling study evaluated the half-cells' cycle life and capacity fade under fast-charging conditions (2C rate). This analysis focused on the cathode compositions that demonstrated the ability to sustain fast-charging conditions during the C-rate tests, specifically 85/5/10, 88/5/7, 90/5/5, and 88/5.18/6.82 using the pressurized cells. Figure 4.9 presents the capacity fade over cycles for all tested cathode compositions using the low-loading cells. Following these graphs, Table 4.3 contains the percentage of the initial experimental capacity concerning the theoretical capacity of the studied cathodes for the same thickness, as well as the capacity fading after 100 and 200 cycles. These capacity fading values were calculated based on the initial experimental capacity of each cell.

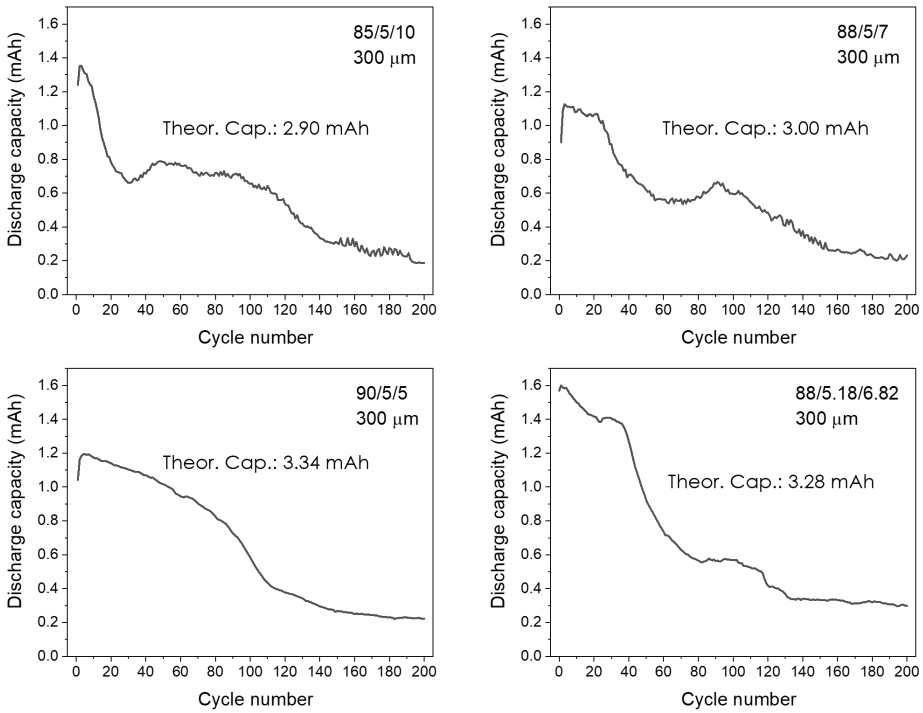


Figure 4.9: Capacity fading with cycles for four different cathode compositions at 2C charging rate and 0.33C discharging rate, using pressurized and low-loading cells.

Table 4.3: Initial capacity regarding the theoretical one, and capacity fading after 100 and 200 cycles for each cathode composition. Low-loading and pressurized cells.

| **Cathode composition** ($CAM/CB/Binder$) | **Initial capacity / Theoretical capacity** (%) | **Capacity fade after 100 cycles** (%) | **Capacity fade after 200 cycles** (%) |
|---|---|---|---|
| 85/5/10 | 46.7 | 51.6 | 86.1 |
| 88/5/7 | 37.5 | 47.1 | 79.5 |
| 90/5/5 | 35.7 | 51.1 | 81.3 |
| 88/5.18/6.82 | 48.8 | 64.4 | 81.4 |

In addition, Figure 4.10 presents the capacity fade over cycles for all tested cathode compositions using the high-loading cells. Following the same procedure as for the low-loading cells, Table 4.4 contains the obtained initial capacity of the cell related to the theoretical one, and the capacity fading after 100 and 200 cycles.

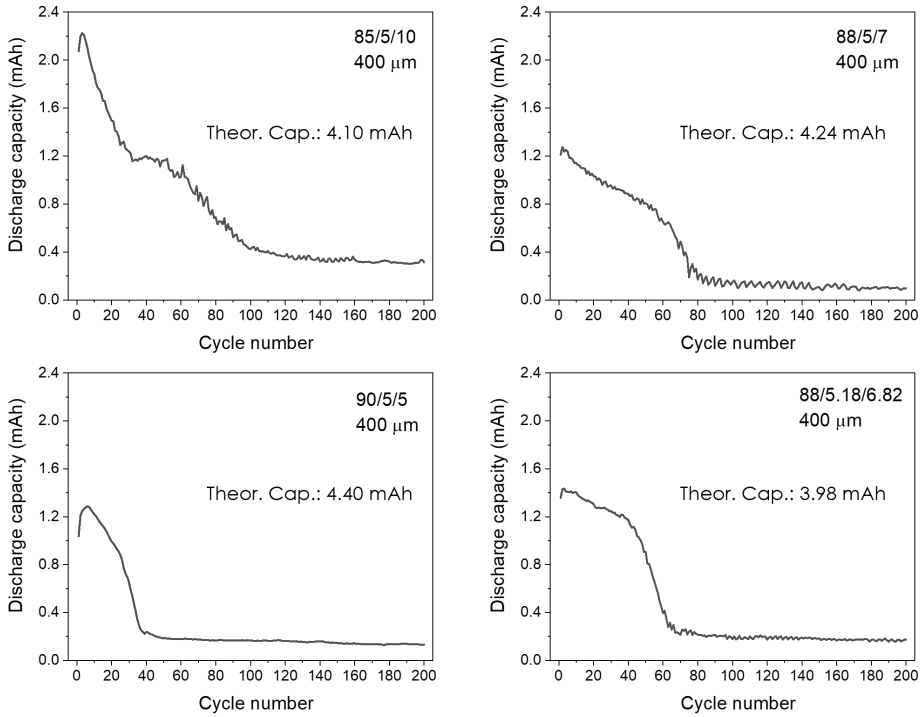


Figure 4.10: Capacity fading with cycles for four different cathode compositions at 2C charging rate and 0.33C discharging rate, using pressurized and high-loading cells.

Table 4.4: Initial capacity regarding the theoretical one, and capacity fading after 100 and 200 cycles for each cathode composition. High-loading and pressurized cells.

| **Cathode composition** ($CAM/CB/Binder$) | **Initial capacity / Theoretical capacity** (%) | **Capacity fade after 100 cycles** (%) | **Capacity fade after 200 cycles** (%) |
|---|---|---|---|
| 85/5/10 | 54.3 | 81.0 | 84.9 |
| 88/5/7 | 29.5 | 88.0 | 92.2 |
| 90/5/5 | 29.2 | 87.1 | 89.8 |
| 88/5.18/6.82 | 36.1 | 87.7 | 87.9 |

Among the tested cathode compositions, the 85/5/10 formulation exhibited the highest initial capacity and the lowest average capacity fading. In contrast, the 88/5.18/6.82 cathode did not achieve comparable performance, suggesting that the previously hypothesized optimal active material-to-carbon black ratio of 17 alone cannot guarantee the best results. Instead, the polymer binder proportion also plays a crucial role, as a higher PVDF content appears to enhance performance, possibly due to improved mechanical integrity and reduced degradation.

These long-term cycling results highlight the importance of an adequate formation step. The coulombic efficiency stabilizes only after 4–5 cycles, while only three formation cycles were applied in this study, suggesting that additional formation cycles may improve initial performance stability.

### b) Cathode Loading Analysis

To better visualise the impact of cathode loading on performance, Table 4.5 reorganizes the parameters analyzed in the previous section, providing a clearer visual representation of the differences between loadings.

Table 4.5: Initial capacity regarding the theoretical one, and capacity fading after 100 and 200 cycles for each studied cathode using pressurized cells.

| **Cathode composition** $(CAM/CB/Binder)$ | **Loading** $(mAh/cm^2)$ | **Initial cap. / Theoretical cap.** (%) | **Capacity fade after 100 cycles** (%) | **Capacity fade after 200 cycles** (%) |
|---|---|---|---|---|
| 85/5/10 | 1.64 | 46.7 | 51.6 | 86.1 |
| | 2.32 | 54.3 | 81.0 | 84.9 |
| 88/5/7 | 1.70 | 37.5 | 47.1 | 79.5 |
| | 2.40 | 29.5 | 88.0 | 92.2 |
| 90/5/5 | 1.89 | 35.7 | 51.1 | 81.3 |
| | 2.49 | 29.2 | 87.1 | 89.8 |
| 88/5.18/6.82 | 1.86 | 48.8 | 64.4 | 81.4 |
| | 2.25 | 36.1 | 87.7 | 87.9 |

With this long-term cycling at a 2C charging rate, it can be concluded that the cathodes with lower loading (thinner cathodes) experience a lower capacity fading and a higher initial capacity than the high-loading ones (thicker cathodes). This trend suggests that optimizing the loading is crucial for achieving the desired performance under fast-charging conditions, and aligns with the results obtained by Yang et al. [19].

## 4.2 Crystal Structure Analysis with XRD

### 4.2.1 Cathode Degradation Analysis

The crystal structure of the NMC811 cathodes was analyzed using XRD. Figure 4.11 presents the diffractogram of the pristine (fresh) 85/5/10 cathode, which is pasted onto the aluminium current collector, along with the diffractogram of the NMC811 powder used in cathode fabrication. These two diffractograms are shown separately because, during coin cell disassembly, while some cathodes remained attached to the aluminium current collector, others had to be scraped off, resulting in a powdered form.

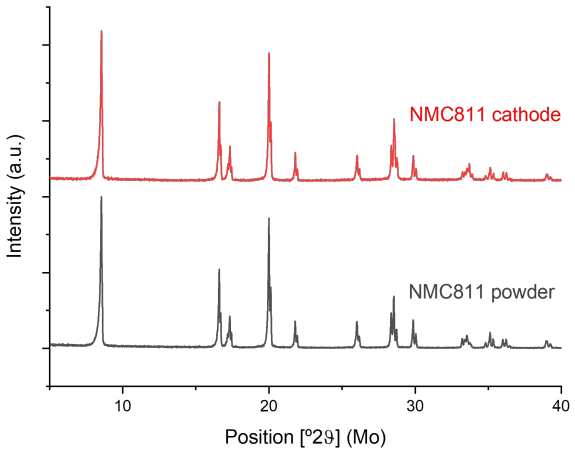


Figure 4.11: Diffractogram of the pristine NMC811 85/5/10 cathode pasted onto the aluminium current collector and the NMC811 fresh powder.

Both diffractograms show identical peak relative intensities and positions, indicating that the aluminium current collector, polymer binder, and carbon black in the cathode (red diffractogram in Figure 4.11) do not influence peak positions or intensity.

To understand these diffractograms, Figure 4.12 also includes the Miller indices for each peak using the pristine 85/5/10 cathode. All these peaks correspond to the layered NMC811 crystal structure (R-3m), and their correspondent Miller indices were obtained using the HighScore Plus software (reference pattern: 96-152-0790) [36]. The results obtained by Kondrakov et al. confirmed these Miller indices [37].

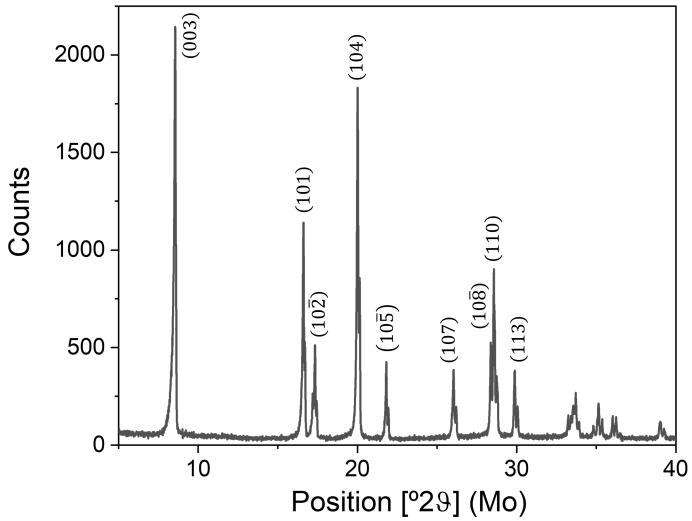


Figure 4.12: Diffractogram of the pristine NMC811 85/5/10 cathode with the corresponding Miller indices.

Figures 4.9 and 4.10 show that the cells exhibited degradation during long-term cycling. To identify the underlying causes of this degradation, an XRD analysis was conducted to compare the crystal structure of the pristine cathodes with that of the EOT cathodes after this long-term cycling. Figure 4.13 shows the comparison between the pristine and EOT 85/5/10 low-loading cathode. Only this diffractogram comparison is shown, as the same results were obtained for all loadings and cathode compositions (included in Appendix B).

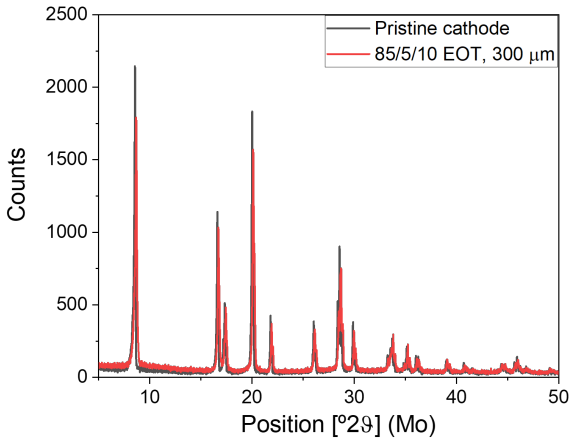


Figure 4.13: Comparison of the diffractograms for the 85/5/10 low-loading cathode before and after long-term cycling.

Since no structural changes were detected in the NMC811 cathode's crystal structure after long-term cycling, the observed capacity fading is likely caused by surface degradation mechanisms rather than bulk material breakdown. This is confirmed by the XRD patterns observed in Figure 4.13, where the peak positions and relative intensities remain unchanged before and after cycling, indicating that the bulk crystal structure is preserved. This suggests that degradation may be driven by interfacial phenomena, such as electrolyte decomposition leading to Cathode–Electrolyte Interphase (CEI) formation, or a loss of electrical contact due to binder instability. Further investigation using EIS or surface-sensitive techniques could help clarify the dominant degradation pathway.

### 4.2.2 Effect of the SOC on the Cathode's Crystal Structure

The crystal structure of the cathode evolves significantly during cycling, as lithium ions are extracted and reinserted. Since the focus is solely on the cathode, SOC is defined here based on lithium extraction (0% SOC corresponds to the fully lithiated state, while 100% SOC represents the fully delithiated cathode). Understanding how the structure changes across different SOC levels is crucial for evaluating phase transitions, structural stability, and potential degradation pathways.

To enable precise control over the charging process and ensure sufficient time for lithium intercalation, the cells were charged at a low rate (0.1C). Additionally, each constant current (CC) step was followed by a 30-minute constant voltage (CV) phase to allow the system to reach equilibrium at the target SOC. This chapter examines the crystal structure at five SOC points: 0%, 25%, 50%, 75%, and 100%, using XRD analysis. Figure 4.14 presents the diffractograms for all SOC levels, enabling a direct comparison of structural features and their evolution throughout the delithiation process. The cathode composition used for this analysis was 85/5/10.

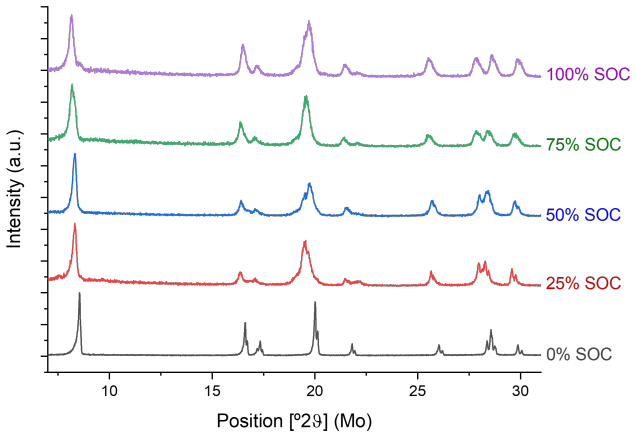


Figure 4.14: Diffractograms of the 85/5/10 cathode at different SOC values.

To more clearly highlight the peak shifts, Figure 4.15 presents zoomed-in sections of different $2\theta$ ranges.

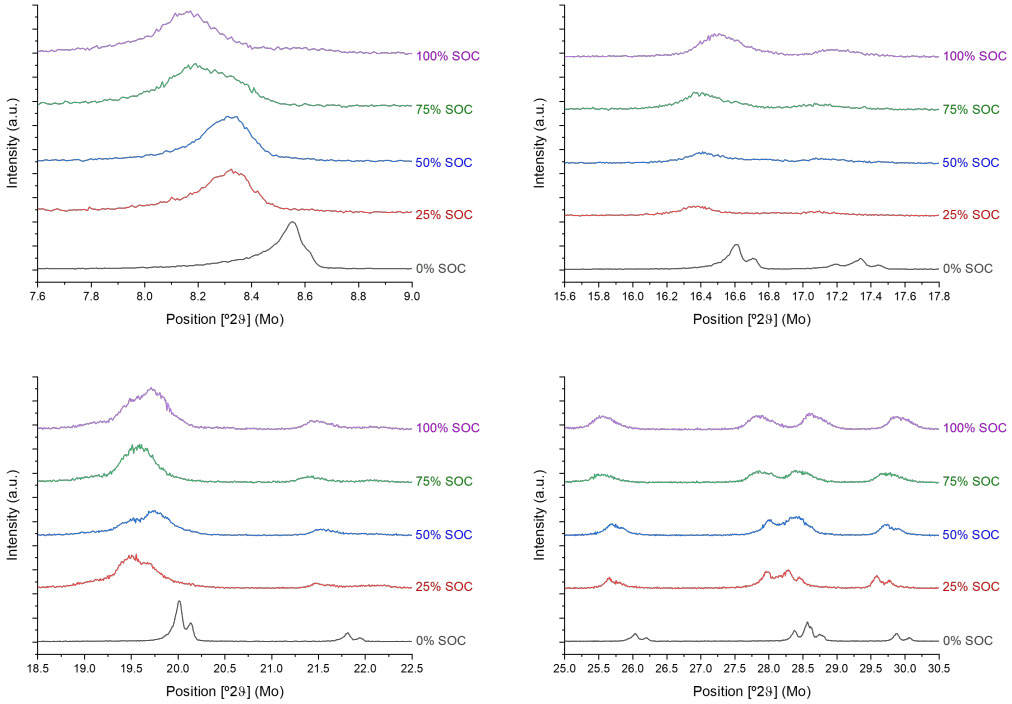


Figure 4.15: Diffractograms for different $2\theta$ ranges and the studied SOC values.

The XRD patterns collected at different SOC levels exhibit a systematic shift in peak positions as delithiation progresses. Specifically, a shift toward lower $2\theta$ values is observed in all the peaks, which indicates lattice expansion during lithium extraction. This behaviour is consistent with previous studies on NCM811, where the removal of lithium reduces electrostatic screening between negatively charged oxygen layers, leading to increased interlayer repulsion and expansion along the c-axis [37]. As described by Kondrakov et al., this expansion continues until approximately x(Li) $\approx$ 0.5, beyond which a contraction of the lattice occurs. This collapse of the interlayer spacing (driven by charge transfer between oxygen and nickel orbitals) is reflected in a shift toward higher $2\theta$ values for the 100% SOC diffractogram in the regions 15.5–18.5° (top-right) and again in 18.5–22.5° (bottom-left), corresponding to a steep decrease in the $c$ lattice parameter and unit cell volume.

Beyond the peak position shifts, changes in width and peak relative intensity are also evident with increasing SOC. The peaks progressively broaden at higher SOC levels, indicating increased microstrain and structural disorder. These trends align with the findings of Kondrakov et al., who reported notable distortion of the layered structure for x(Li) $<$ 0.5 [37].

The evolution of the (003)/(101) and (003)/(104) XRD intensity ratios in NMC811 across different SOC reveals notable structural changes during electrochemical cycling. Table 4.6 shows these relative intensities of these peaks.

Table 4.6: Relative intensities of the peaks (003)/(101) and (003)/(104) for each SOC value.

| **Peaks** | **0% SOC** | **25% SOC** | **50% SOC** | **75% SOC** | **100% SOC** |
|---|---|---|---|---|---|
| (003)/(101) | 1.9 | 4.3 | 3.8 | 2.5 | 1.9 |
| (003)/(104) | 1.2 | 1.4 | 1.9 | 1.2 | 1.1 |

The pronounced increase in the (003)/(101) ratio at low-to-moderate SOC suggests a transient improvement in layered ordering, likely due to reduced Li/Ni cation mixing and expansion of the c-axis upon initial delithiation. As charging progresses beyond 50% SOC, the subsequent decrease

in both intensity ratios is consistent with the onset of structural densification, partial c-axis collapse, and possibly renewed Ni migration into Li layers. The more significant variation in the (003)/(101) ratio compared to (003)/(104) reflects the higher sensitivity of the (003) and (101) reflections to interlayer disorder and anisotropic lattice strain, as well as potential contributions from preferred orientation effects. Overall, these trends underscore the intimate link between electrochemical state and crystallographic order in Ni-rich layered cathodes [38].

Overall, the evolution of the XRD patterns together with the EOT diffractogram (Figure 4.13) confirm a progressive and reversible structural transformation in the cathode material, closely linked to lithium content and driven by redox activity and charge-transfer phenomena.

## 4.3 Pouch Full-Cell Performance

The highest-performing cathode composition among those studied (85/5/10) was selected to fabricate the pouch full-cells. A cathode coating on an aluminium current collector with a wet thickness of 400 µm was produced, adapted to use with pouch cells, and tested. Cells with two different N/P ratios were assembled: 1.19 and 1.25.

### 4.3.1 Impact of the Charging Rate

This section investigates the impact of varying charging rates on the discharge capacity of the pouch cell. As shown in Figure 4.16, the charge and discharge profiles at two different charging rates, 1C and 0.1C, are compared to highlight the relationship between charging rate and capacity retention. The upper cut-off potential is the same for the two cases: 4.2 V. The pouch cell used for this study has an N/P ratio of 1.25.

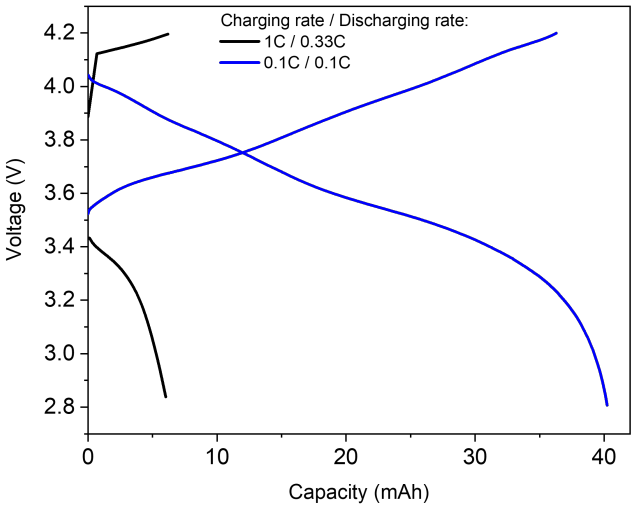


Figure 4.16: Potential vs capacity graph for different charging/discharging rates. Upper cut-off potential: 4.2 V.

The results depicted in Figure 4.16 demonstrate that the discharge capacity decreases as the charging rate increases. This trend was also observed in the C-rate study of the coin half-cells, and it can be attributed to several factors, including increased internal resistance at higher charging rates, which leads to less efficient ion diffusion within the electrode materials. As the charging rate increases, the time available for lithium-ion migration decreases, resulting in an incomplete charge transfer and a reduced overall capacity. Therefore, fast-charging conditions, while improving charging times, can negatively impact the long-term performance and efficiency of lithium-ion batteries.

### 4.3.2 Impact of Long-Term Cycling

The single-layer pouch cells were unable to support fast-charging conditions (2C rate), likely due to limitations in the electrolyte formulation, which may not be optimal for high-rate operation in this cell format. As a result, Figure 4.17.a illustrates the capacity fading of a pouch cell with an N/P ratio of 1.19 under a 1C charging and 0.33C discharging regime. In parallel, Figure 4.17.b shows the evolution of the coulombic efficiency over the same cycling period, offering further insights into the reversibility and stability of the electrochemical processes occurring during long-term cycling.

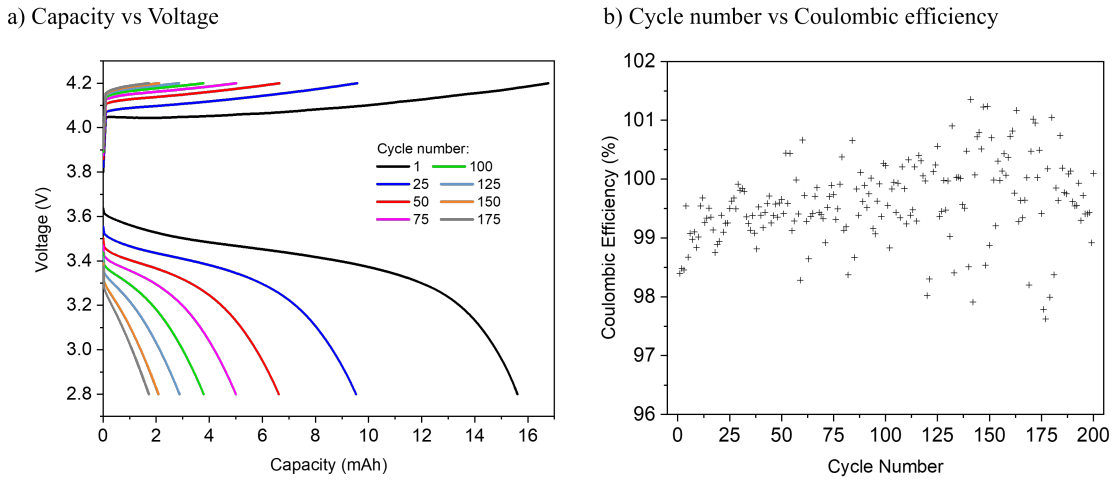


Figure 4.17: Long-term performance of the pouch cell: (a) capacity vs voltage for different cycle numbers and (b) cycle number vs CE.

The long-term cycling results under a 1C charging and 0.33C discharging protocol reveal a marked degradation in capacity over time. Starting from a value already below 50% of the cell's theoretical capacity (47.7 mAh), the discharge capacity continues to decline steadily with increasing cycle number. This pronounced capacity fading indicates that fast charging imposes considerable stress on the cell, likely leading to lithium plating, active lithium loss, and structural or interfacial degradation.

Figure 4.17.b displays the evolution of the CE during long-term cycling. While the average CE remains close to 100% throughout the test, an increasing dispersion of the data points is observed as the number of cycles progresses. This growing fluctuation suggests that the electrochemical processes become less stable over time. The rising variability could be attributed to intermittent side reactions such as lithium plating or localized SEI instability, which may not occur uniformly during every cycle but still impact long-term cell behaviour. These fluctuations, when paired with the capacity fading observed in Figure 4.17.a, hint an underlying degradation mechanisms that manifest sporadically yet progressively compromise cell performance. Therefore, the increase in CE dispersion can serve as an early indicator of cycling-induced instabilities that precede more severe and irreversible forms of degradation.

### 4.3.3 Impact of the Upper Cut-Off Potential

A separate study was conducted on the N/P = 1.25 pouch cell to evaluate how varying the upper cut-off potential influences the discharge capacity. The potentials examined were 4.2 V, 4.3 V, 4.4 V, 4.5 V, and 4.6 V. As illustrated in Figure 4.18, the discharge capacity increases with a higher upper cut-off potential. This analysis employed a charging rate of 1C and a discharging rate of 0.33C.

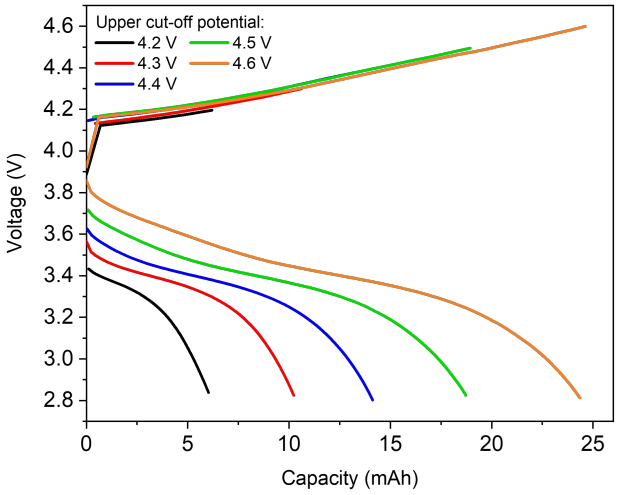


Figure 4.18: Potential vs capacity graph for different upper cut-off potential values. 1C charging rate, 0.33C discharging rate.

From the plotted data, it is evident that raising the upper cut-off potential leads to a higher discharge capacity. This behaviour can be attributed to the deeper delithiation of the cathode at elevated voltages, which increases the fraction of active material accessed during cycling.

Although higher upper cut-off potentials are often associated with increased degradation, the results obtained in this study suggest otherwise. As shown in Figure 4.19, the capacity fade after 100 cycles at 4.6 V is 70.55%, which is comparable to the 75.55% fade observed at 4.2 V (Figure 4.17.a). This indicates that operating at 4.6 V does not significantly accelerate capacity loss over 100 cycles. However, post-mortem analysis revealed signs of corrosion in the aluminium tab at the higher voltage. This suggests that, despite similar capacity retention, elevated voltages may still induce detrimental chemical effects at the electrode–electrolyte interface, particularly affecting current collector stability. Therefore, ensuring the long-term integrity of cell components remains a key consideration when operating at high voltages.

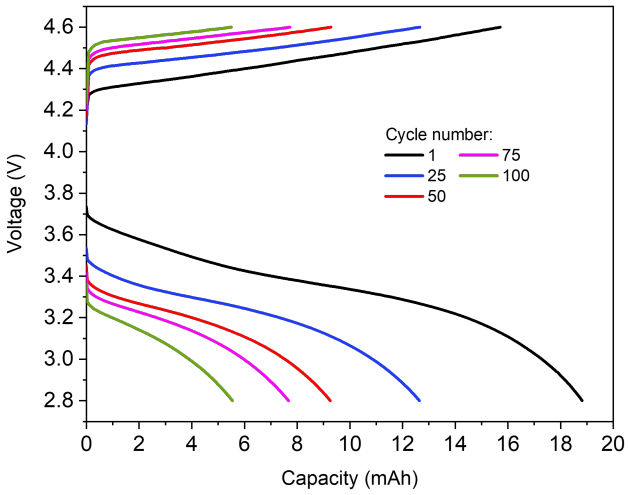


Figure 4.19: Long-term performance of the pouch cell using 4.6 V as upper cut-off potential.

### 4.3.4 EIS Analysis: Pouch Full-Cell vs. Coin Half-Cell Performance

To better understand the origin of the fast-charging limitations observed in the pouch full-cells, an EIS study was performed on both the pouch full-cell and the coin half-cell configurations after their activation. These two systems differ not only in geometry but also in electrode composition: the coin half-cell employs lithium metal as the counter electrode, while the pouch full-cell uses graphite as the anode. Interestingly, only the coin half-cell was capable of sustaining a 2C charging rate, whereas the pouch full-cell could not.

EIS measurements were therefore used to evaluate the electrochemical characteristics of each system in order to identify possible resistive or diffusive bottlenecks that might explain their contrasting behaviours. The Nyquist plots presented in Figure 4.20 and the values in Table 4.7 provide insight into the charge transfer resistance, ion transport characteristics, and capacitance effect of each configuration. The EEC used for this analysis is the same as the one used for the previous pressure analysis (Figure 4.5). In this case, since the two cells being compared have different electrode areas, both the Nyquist plots and the values in Table 4.7 were calculated by normalizing to the cathode area. As the units of the relevant parameters are based on resistance, they were multiplied by the electrode area to obtain specific values in $\Omega \cdot \mathrm{cm}^2$.

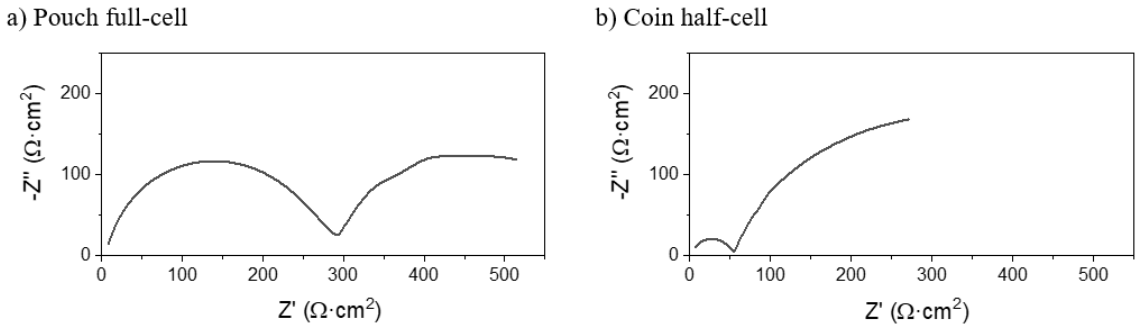


Figure 4.20: Nyquist plot of (a) the pouch full-cell and (b) the coin half-cell for the 85/5/10 cathode composition and high-loading after cell activation.

Table 4.7: Comparison of the charge transfer resistance, the Warburg impedance, and capacitance effect for the pouch full-cell and the coin half-cell, using the 85/5/10 cathode.

| **Cell type** | **Cathode area** ($cm^2$) | $\mathbf{R_{ct}}$ ($\Omega{\cdot}cm^2$) | **W** ($\Omega{\cdot}cm^2/\sqrt{s}$) | $\mathbf{C_{dl}}$ ($\mu F/cm^2$) |
|---|---|---|---|---|
| Pouch full-cell | 24.08 | 252.82 | 166.15 | 1.27 |
| Coin half-cell | 1.77 | 40.36 | 133.28 | 1.53 |

The EIS results clearly highlight significant differences in the electrochemical behavior of the pouch full-cell and the coin half-cell, which help explain their contrasting performances under fast-charging conditions. The pouch full-cell exhibits a much higher charge transfer resistance (252.82 $\Omega \cdot \mathrm{cm}^2$) compared to the coin half-cell (40.36 $\Omega \cdot \mathrm{cm}^2$), as shown in Table 4.7. This elevated $\mathrm{R_{ct}}$ indicates more sluggish interfacial charge transfer kinetics in the pouch cell, which can significantly hinder its ability to sustain high current rates such as a 2C fast charge. Furthermore, the Warburg impedance, which reflects ion diffusion limitations, is also higher in the pouch full-cell (166.15 $\Omega{\cdot}\mathrm{cm}^2 / \sqrt{s}$) than in the coin half-cell (133.28 $\Omega{\cdot}\mathrm{cm}^2 / \sqrt{s}$), suggesting that the pouch configuration experiences greater mass transport resistance.

The double-layer capacitance values per unit area are relatively similar for both systems indicating comparable interfacial capacitance. The Nyquist plots in Figure 4.20 support the quantitative data,

with the pouch cell displaying a significantly larger semicircle and total impedance, confirming the presence of substantial resistive and diffusional limitations. These findings suggest that the pouch full-cell configuration is not well-suited for fast-charging at a 2C rate, while the coin half-cell, with lower charge transfer and diffusion resistances, can accommodate higher charging rates more effectively.

# Chapter 5

# Conclusion

**Summary of Key Findings**

This thesis has demonstrated the critical role of cathode optimization in enhancing the fast-charging capabilities of LiBs based on NMC811. Through systematic experimentation using coin half-cells, the study has explored the influence of various parameters on electrochemical performance and long-term stability. The results highlight the significance of fine-tuning electrode composition, loading, and mechanical constraints to achieve optimal battery behaviour under high C-rate conditions.

A key finding of this work is the importance of cathode composition in determining the mechanical and electrochemical stability of the electrodes. The study establishes that maintaining a minimum of 5 wt% polymer binder (PVDF) is essential to prevent mechanical degradation while ensuring good ionic and electronic conductivity. Furthermore, the optimal active material-to-carbon black ratio to sustain fast-charging conditions was identified as 17, which gives enough carbon black quantity to make the electron transport effective. The cathode composition with the best results was 85/5/10, demonstrating an optimal balance between electrochemical performance and durability. These findings provide crucial guidelines for the formulation of cathodes that sustain fast-charging conditions without compromising long-term performance.

In addition to composition, cathode loading plays a significant role in determining both initial capacity and degradation behaviour. The experimental results indicate that low-loading cathodes exhibited higher initial capacity and lower capacity fading compared to high-loading cathodes. This suggests that reducing the electrode thickness helps in maintaining structural integrity and mitigating long-term degradation effects. On the other hand, high-loading cathodes, while offering greater total energy storage, suffer from increased charge transfer resistance and diffusion limitations, which negatively impact their cycle life. The balance between these factors is essential for optimizing both energy density and long-term performance in fast-charging applications.

Another major contribution of this study is the demonstrated improvements achieved by applying pressure to the cells through the addition of a second spring in the coin cell assembly. The results show that pressurized cells exhibit significantly reduced charge transfer resistance and Warburg impedance, indicating improved ion transport and electrochemical kinetics. This enhancement is attributed to better electrode-electrolyte contact and minimized porosity variations under compressive force, which lead to a more stable and uniform reaction environment. These findings underscore the importance of mechanical constraints in optimizing battery performance and pave the way for further studies on pressure-assisted electrode assembly techniques.

The ex-situ XRD analysis provided additional insights into the degradation mechanisms of the cathodes. The results indicated that there were no changes in the crystal structure of the cathodes after long-term cycling. This suggests that the primary degradation mechanisms observed in the cells are not related to structural transformations within the NMC811 material. Instead, other factors such as electrode-electrolyte interactions or surface-side reactions may play a more dominant

role in the capacity fading observed over extended cycling.

In this work, while coin half-cells employing a lithium metal counter electrode were shown to sustain high charging rates, pouch full-cells with graphite anodes exhibited clear limitations under 2C charging conditions. This behavior is supported by electrochemical impedance spectroscopy, which revealed that the pouch full-cells had significantly higher charge transfer resistance and Warburg impedance compared to the coin half-cells. These results indicate that both interfacial kinetics and ion diffusion are more hindered in the pouch configuration, likely due to differences in electrode architecture, cell design, and overall mass transport pathways. In contrast, the coin half-cells demonstrated lower resistance and better ion transport behavior, allowing them to accommodate fast-charging more effectively.

**Experimental Limitations**

While the findings provide useful guidelines for designing fast-charging electrodes, certain limitations must be acknowledged. Firstly, all tests were conducted at room temperature, whereas temperature variations (particularly in electric vehicle operation) can significantly affect battery performance and degradation behaviour. Secondly, long-term cycling was limited to 200 cycles, which is insufficient to fully assess calendar ageing or long-term capacity retention.

Furthermore, the electrodes were fabricated using lab-scale, manual processes, introducing variability not typically present in industrial roll-to-roll production. This discrepancy may affect the reproducibility of results at scale. Lastly, only single-layer pouch cells were tested; hence, the impact of electrode design and composition in multi-layer or high-capacity cell stacks remains unexplored.

**Comparison with Recent Literature**

The results of this thesis are consistent with recent studies investigating the high-rate capabilities of Ni-rich cathodes. In particular, Yang et al. reported that thinner electrodes exhibit improved fast-charging performance due to reduced lithium-ion transport limitations and enhanced electronic conductivity [19]. These findings align with the trends observed in this work, where thinner electrodes outperformed thicker ones under fast-charging conditions. However, no recent literature specifically addressing the cathode composition comparison carried out in this study, or the performance of pressurized cell configurations under fast-charging conditions, was found for comparison.

**Future Work**

Future research should address several open challenges to further advance the development of fast-charging LiBs. Incorporating in-situ or operando characterization techniques like synchrotron-based XRD would allow real-time monitoring of structural evolution and degradation mechanisms during high-rate cycling. Testing performance under low and high temperature conditions could provide a more comprehensive understanding of battery behaviour in realistic operating environments.

Moreover, scaling up the electrode fabrication and testing of multi-layer pouch cells would offer insights into industrial viability and help bridge the gap between lab-scale optimization and commercial application. In parallel, the integration of artificial intelligence (AI) and machine learning (ML) tools could significantly accelerate electrode optimization by enabling predictive modeling based on composition, processing parameters, and performance data. These data-driven approaches can help identify optimal configurations, reduce experimental time, and enhance understanding of degradation trends across large datasets.

# Declaration of Generative AI and AI-assisted Technologies in the Writing Process

During the preparation of this work, the author used ChatGPT in order to improve the translation and to assist in writing a clearer and more cohesive text. After using this tool/service, the author reviewed and edited the content as needed and takes full responsibility for the content of the publication.

# Bibliography


[1] G. A. Mansoori, L. B. Agyarko, L. A. Estevez, *et al.*, "Fuels of the future for renewable energy sources (ammonia, biofuels, hydrogen)," Tech. Rep., 2021.

[2] U. Datta, A. Kalam, and J. Shi, *A review of key functionalities of battery energy storage system in renewable energy integrated power systems*, Oct. 2021. DOI: 10.1002/est2.224.

[3] E. Commission. "Emissions database for global atmospheric research." (2024), [Online]. Available: https://edgar.jrc.ec.europa.eu/report_2024#sources (visited on 12/04/2024).

[4] *Global ev outlook 2024*, Apr. 2024. [Online]. Available: https://www.iea.org/reports/global-ev-outlook-2024/trends-in-electric-cars (visited on 10/04/2024).

[5] C. M. A. Brett and A. M. O. Brett, *Electrochemistry : principles, methods, and applications*. Oxford University Press, 1993, p. 427, ISBN: 0198553897.

[6] Y. Liu, M. Y. Su, Z. Y. Gu, *et al.*, *Advanced lithium primary batteries: Key materials, research progresses and challenges*, Oct. 2022. DOI: 10.1002/tcr.202200081.

[7] E. Faegh, T. Omasta, M. Hull, *et al.*, "Understanding the dynamics of primary zn-mno 2 alkaline battery gassing with operando visualization and pressure cells," *Journal of The Electrochemical Society*, vol. 165, A2528–A2535, 11 2018, ISSN: 0013-4651. DOI: 10.1149/2.0321811jes.

[8] X. Yu, Y. Fu, X. Cai, *et al.*, "Flexible fiber-type zinc-carbon battery based on carbon fiber electrodes," *Nano Energy*, vol. 2, pp. 1242–1248, 6 Nov. 2013, ISSN: 22112855. DOI: 10.1016/j.nanoen.2013.06.002.

[9] M. Morris, "Comparison of rechargeable battery technologies," *ASME Early Career Technical Journal*, vol. 11, pp. 148–155, Nov. 2012.

[10] T. B. Reddy, "Linden's handbook of batteries," Tech. Rep.

[11] H. Budde-Meiwes, J. Drillkens, B. Lunz, *et al.*, *A review of current automotive battery technology and future prospects*, 2013. DOI: 10.1177/0954407013485567.

[12] E. Hossain, H. M. R. Faruque, M. S. H. Sunny, N. Mohammad, and N. Nawar, "A comprehensive review on energy storage systems: Types, comparison, current scenario, applications, barriers, and potential solutions, policies, and future prospects," *Energies*, vol. 13, no. 14, 2020, ISSN: 1996-1073. DOI: 10.3390/en13143651. [Online]. Available: https://www.mdpi.com/1996-1073/13/14/3651.

[13] A. A. Nkembi, M. Simonazzi, D. Santoro, P. Cova, and N. Delmonte, "Comprehensive review of energy storage systems characteristics and models for automotive applications," *Batteries*, vol. 10, no. 3, 2024, ISSN: 2313-0105. DOI: 10.3390/batteries10030088. [Online]. Available: https://www.mdpi.com/2313-0105/10/3/88.

[14] S. Ahmed, I. Bloom, A. N. Jansen, *et al.*, "Enabling fast charging – a battery technology gap assessment," *Journal of Power Sources*, vol. 367, pp. 250–262, Nov. 2017, ISSN: 03787753. DOI: 10.1016/j.jpowsour.2017.06.055.

[15] O. Toprakçı, H. A. K. TOPRAKCI, L. Ji, and X. Zhang, "Cheminform abstract: Fabrication and electrochemical characteristics of lifepo4 powders for lithium-ion batteries," *ChemInform*, vol. 42, Sep. 2011. DOI: 10.1002/chin.201143199.

[16] R. Collin, Y. Miao, A. Yokochi, P. Enjeti, and A. V. Jouanne, "Advanced electric vehicle fast-charging technologies," *Energies*, vol. 12, 10 2019, ISSN: 19961073. DOI: 10.3390/en12101839.

[17] Y. Miao, P. Hynan, A. von Jouanne, and A. Yokochi, "Current li-ion battery technologies in electric vehicles and opportunities for advancements," *Energies*, vol. 12, pp. 1074–1094, Mar. 2019. DOI: 10.3390/en12061074.

[18] M. Thackeray, W. David, P. Bruce, and J. Goodenough, "Lithium insertion into manganese spinels," *Materials Research Bulletin*, vol. 18, no. 4, pp. 461–472, 1983, ISSN: 0025-5408. DOI: https://doi.org/10.1016/0025-5408(83)90138-1. [Online]. Available: https://www.sciencedirect.com/science/article/pii/0025540883901381.

[19] Z. Yang, H. Charalambous, Y. Lin, *et al.*, "Extreme fast charge aging: Correlation between electrode scale and heterogeneous degradation in ni-rich layered cathodes," *Journal of Power Sources*, vol. 521, Feb. 2022, ISSN: 03787753. DOI: 10.1016/j.jpowsour.2021.230961.

[20] M. Greenwood, M. Wentker, and J. Leker, "A region-specific raw material and lithium-ion battery criticality methodology with an assessment of nmc cathode technology," *Applied Energy*, vol. 302, Nov. 2021, ISSN: 03062619. DOI: 10.1016/j.apenergy.2021.117512.

[21] T. R. Tanim, Z. Yang, D. P. Finegan, *et al.*, "A comprehensive understanding of the aging effects of extreme fast charging on high ni nmc cathode," *Advanced Energy Materials*, vol. 12, 22 Jun. 2022, ISSN: 16146840. DOI: 10.1002/aenm.202103712.

[22] A. K. Mishra, Monika, and B. S. Patial, "A review on recent advances in anode materials in lithium ion batteries," *Materials Today Electronics*, vol. 7, May 2024, ISSN: 27729494. DOI: 10.1016/j.mtelec.2024.100089.

[23] H. Hossain, M. Islam, M. Chowdhury, and N. Hossain, "Prospects and challenges of anode materials for lithium-ion batteries - a review," *Cleaner Energy Systems*, vol. 9, p. 100 145, Sep. 2024. DOI: 10.1016/j.cles.2024.100145.

[24] T. F. Yi, L. J. Jiang, J. Shu, C. B. Yue, R. S. Zhu, and H. B. Qiao, "Recent development and application of li4ti5o 12 as anode material of lithium ion battery," *Journal of Physics and Chemistry of Solids*, vol. 71, pp. 1236–1242, 9 Sep. 2010, ISSN: 00223697. DOI: 10.1016/j.jpcs.2010.05.001.

[25] E. Technologies, *Guide to anode materials in lithium-ion batteries*. [Online]. Available: https://www.echiontech.com/insights/guide-to-anode-materials-in-lithium-ion-batteries (visited on 03/21/2025).

[26] S. Hemavathi, S. Srirama, and A. S. Prakash, *Present and future generation of secondary batteries: A review*, Dec. 2023. DOI: 10.1002/cben.202200040.

[27] M. Li, M. Feng, D. Luo, and Z. Chen, *Fast charging li-ion batteries for a new era of electric vehicles*, Oct. 2020. DOI: 10.1016/j.xcrp.2020.100212.

[28] T. R. Tanim, P. J. Weddle, Z. Yang, *et al.*, *Enabling extreme fast-charging: Challenges at the cathode and mitigation strategies*, Dec. 2022. DOI: 10.1002/aenm.202202795.

[29] F. Wu, J. Ma, Y. Chen, *et al.*, "Progress and perspectives of high-energy and high-power cathode materials for rechargeable lithium-ion batteries," *Journal of Power Sources*, vol. 448, p. 227 401, 2020. DOI: 10.1016/j.jpowsour.2019.227401.

[30] W. Mai, A. M. Colclasure, and K. Smith, "Model-instructed design of novel charging protocols for the extreme fast charging of lithium-ion batteries without lithium plating," *Journal of The Electrochemical Society*, vol. 167, p. 080 517, 8 May 2020, ISSN: 19457111. DOI: 10.1149/1945-7111/ab8c84.

[31] M. Kim and J. Kim, "Advanced integrated fast-charging protocol for lithium-ion batteries by considering degradation," *ACS Sustainable Chemistry and Engineering*, vol. 12, pp. 6786–6796, 17 Apr. 2024, ISSN: 21680485. DOI: 10.1021/acssuschemeng.4c01673.

[32] A. V. Llewellyn, A. Matruglio, D. J. Brett, R. Jervis, and P. R. Shearing, *Using in-situ laboratory and synchrotron-based x-ray diffraction for lithium-ion batteries characterization: A review on recent developments*, Dec. 2020. DOI: 10.3390/condmat5040075.

[33] F. Friedrich, B. Strehle, A. T. S. Freiberg, *et al.*, "Editors' choice—capacity fading mechanisms of ncm-811 cathodes in lithium-ion batteries studied by x-ray diffraction and other diagnostics," *Journal of The Electrochemical Society*, vol. 166, A3760–A3774, 15 2019, ISSN: 0013-4651. DOI: 10.1149/2.0821915jes.

[34] R. M. Salgado, F. Danzi, J. E. Oliveira, A. El-Azab, P. P. Camanho, and M. H. Braga, *The latest trends in electric vehicles batteries*, Jun. 2021. DOI: 10.3390/molecules26113188.

[35] W. Choi, H. C. Shin, J. M. Kim, J. Y. Choi, and W. S. Yoon, *Modeling and applications of electrochemical impedance spectroscopy (eis) for lithium-ion batteries*, Feb. 2020. DOI: 10.33961/jecst.2019.00528.

[36] H. Arai, M. Tsuda, and Y. Sakurai, "Lithium nickelate electrodes with enhanced high-temperature performance and thermal stability," Tech. Rep., 2000, pp. 76–81. [Online]. Available: www.elsevier.comrlocaterjpowsour.

[37] A. O. Kondrakov, H. Geßwein, K. Galdina, *et al.*, "Charge-transfer-induced lattice collapse in ni-rich ncm cathode materials during delithiation," *Journal of Physical Chemistry C*, vol. 121, 39 2017, ISSN: 19327455. DOI: 10.1021/acs.jpcc.7b06598.

[38] E. D. Orlova, A. A. Savina, S. A. Abakumov, A. V. Morozov, and A. M. Abakumov, "Comprehensive study of li+/ni2+ disorder in ni-rich nmcs cathodes for li-ion batteries," *Symmetry*, vol. 13, 9 Sep. 2021, ISSN: 20738994. DOI: 10.3390/sym13091628.

# A Carbon Nanotubes (CNTs) Coating Results

An additional study was conducted to evaluate the effect of applying a CNT coating on top of the cathode. However, due to the poor performance observed, the results were not included in the main body of the thesis. Instead, Appendix A presents the outcomes obtained from the coin half-cells incorporating the CNT-coated cathodes.

## A.1 C-rate Testing Results

Figure A.1 shows the C-rate testing results for the following cells: the first column presents a 90/5/5 cathode with a 100 µm wet coating of CNTs, the second an 85/5/10 cathode with a 50 µm wet CNT coating, and the last an 85/5/10 cathode with a 20 µm wet CNT coating. The thickness values in each figure refer to the wet coating thicknesses applied during fabrication.

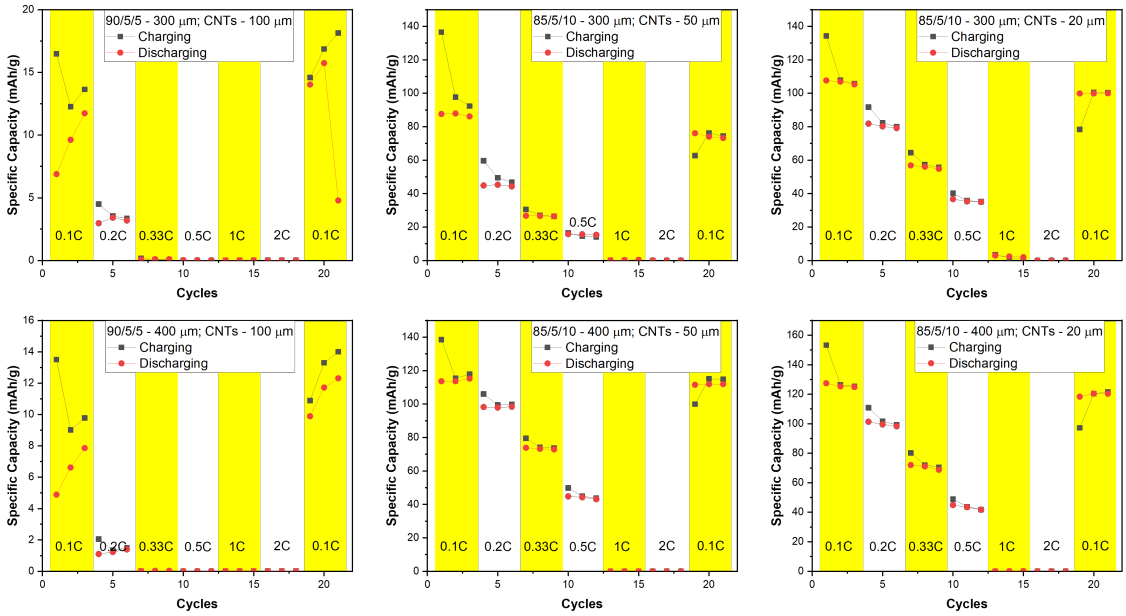


Figure A.1: C-rate testing for the different CNTs coatings.

## A.2 EIS Results

Figure A.2 shows the Nyquist plots corresponding to the previous results.

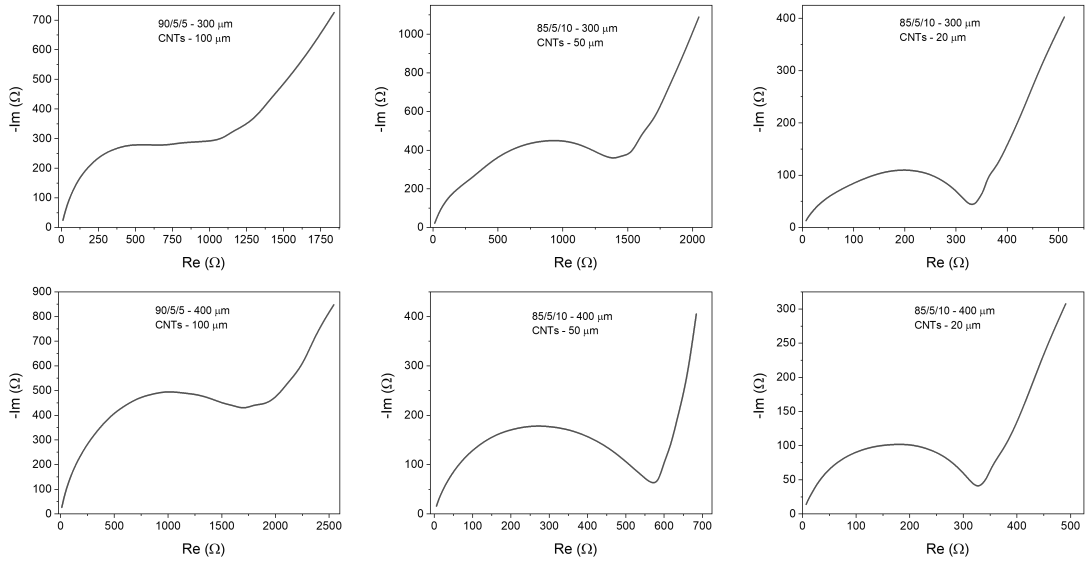


Figure A.2: Nyquist plot of the coin half-cells with a CNT coating on top of the cathode.

The poor performance can clearly be attributed to the significantly high resistance observed in the Nyquist plots. The results suggest that the electrochemical performance of the cells improves as the CNTs coating thickness decreases. This enhancement can be attributed to the reduced resistance for lithium-ion diffusion through the coating layer. A thinner CNT coating offers a shorter and less resistive path for ion transport, facilitating better kinetics during charge and discharge processes.

# B XRD Complementary Results

This Appendix B presents the ex-situ XRD diffractograms obtained that were not presented in the main body of this thesis. Figure B.1 shows the comparison between the fresh and the tested cathode after the long-term testing for the three cathode compositions that were not presented.

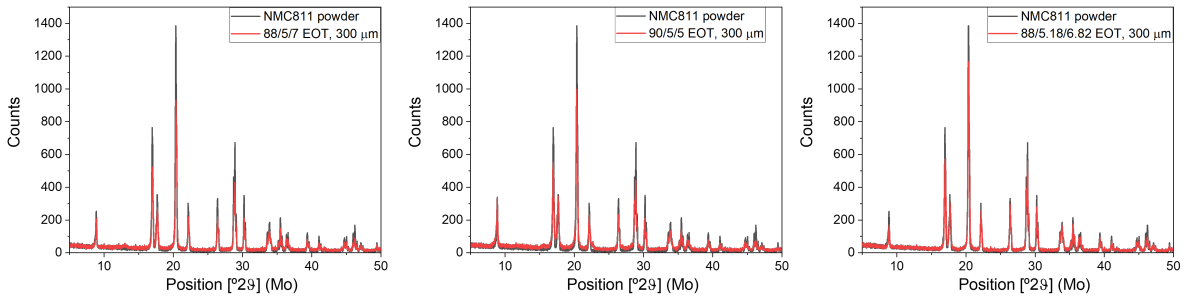


Figure B.1: Comparison of the diffractograms for the low-loading cathodes before and after long-term cycling.

In this case, the peak at $2\theta = 8°$ appears with lower intensity than the one shown in Figure 4.13. This is because the cathodes were detached from the aluminium current collector during disassembly, and the thick sample holder used for the powder analysis reduced the detected intensity of this peak. Nevertheless, the diffractograms are essentially identical to the one in Figure 4.13, indicating that there are no changes in the cathode's crystal structure after the long-term cycling, as previously mentioned.

# C High Temperature Analysis

This Appendix C presents the results obtained with the coin full-cells at 45 °C for a long-term cycling at 2C charging rate. Figure C.1 shows the capacity fading with cycles for the two studied cathode compositions and for low and high loading: 85/5/10 and 88/5.18/6.82.

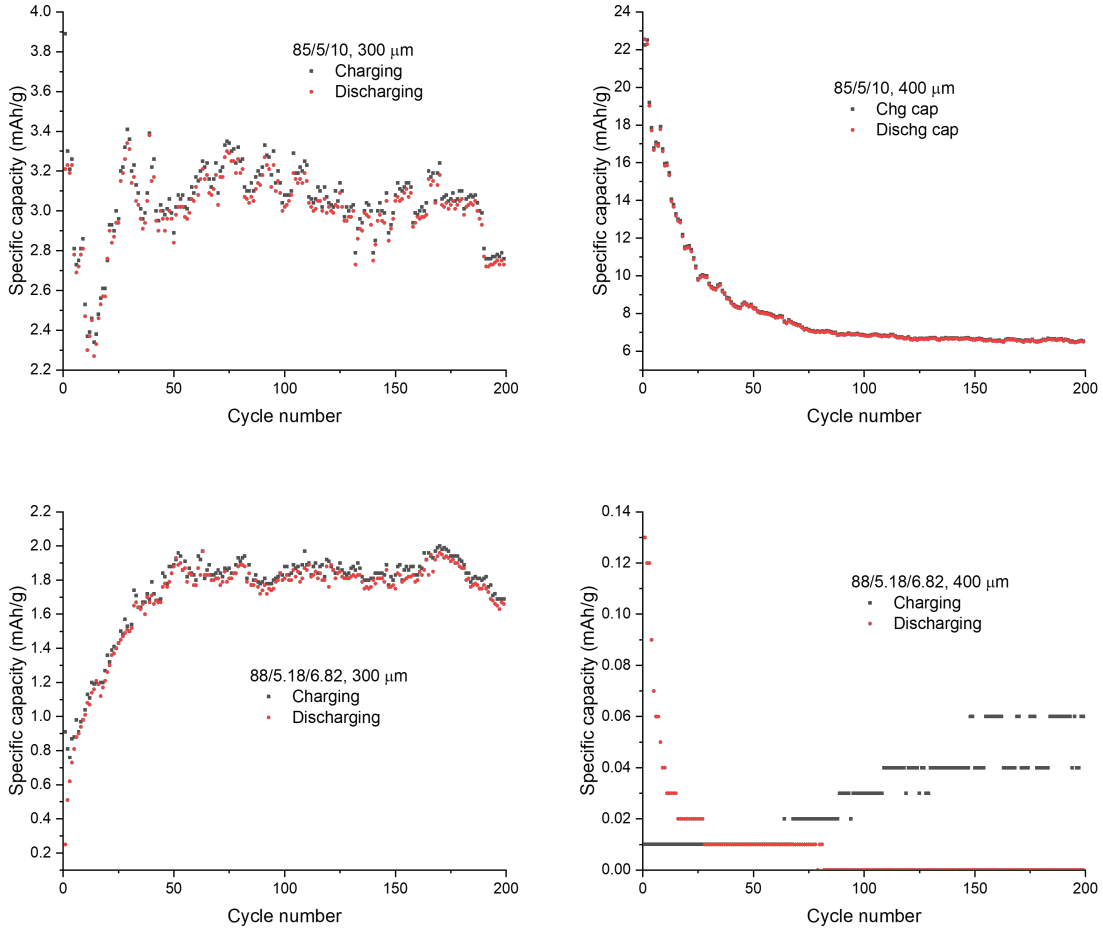


Figure C.1: Capacity fading with cycles of the coin full-cells at 45 °C.

The results presented in this figure exhibit notably low capacity values when compared to the theoretical capacity of about 200 mAh/g, indicating poor electrochemical performance. It is important to note that these tests were conducted using coin full-cells with graphite as the anode, whereas the rest of the thesis relies on half-cell configurations. Additionally, these experiments were performed at 45 °C, in contrast to the room temperature conditions used throughout the main study. These differences in cell configuration and testing temperature likely contributed to

the observed deviations and are included here for completeness.